

## Using Astrometry to Break Degeneracies in Stellar Surface Mapping

JAMILA S. TAAKI ,<sup>1</sup> LIA CORRALES ,<sup>2</sup> AND ALFRED O. HERO III ,<sup>3</sup>

<sup>1</sup> Michigan Institute for Data Science, University of Michigan  
 500 S State St, Ann Arbor, MI 48109

<sup>2</sup> Department of Astronomy, University of Michigan  
 West Hall, 1085 S. University, Ann Arbor, MI 48109

<sup>3</sup> Department of Electrical Engineering and Computer Science, University of Michigan  
 1301 Beal Avenue, Ann Arbor, MI 48109

### ABSTRACT

Astrometric jitter noise arises when starspots on a rotating stellar surface move in and out of view, shifting the photocenter. This noise may limit our ability to detect and weigh small, sub-Neptune-sized planets around active stars. By deriving a linear forward model for the astrometric jitter signal of a rotating star in a spherical-harmonic coordinate system, we show that jitter noise can be used to reconstruct surface-brightness maps and, in principle, disentangle jitter from stellar reflex motion. Furthermore, we show that astrometry and photometry probe complementary stellar surface information: photometry measures even-degree spherical harmonic surfaces that are symmetric about the equator, while astrometry measures odd-degree modes. Their joint use, therefore, breaks degeneracies in stellar surface mapping. Our model further quantifies the variation in the astrometric signal with inclination angle, which is foundational for studies of worst-case configurations of astrometric star-spot noise. For example, we show that pole-on stellar inclinations lead to poorly constrained inversions, as any stellar surface produces a purely circular astrometric jitter signal. We characterize the degeneracy in jointly identifying the stellar surface and stellar inclination, and develop a surface estimation approach. Using this approach, we present example simulations and reconstructions that demonstrate the use of astrometry data alongside light-curve data to improve stellar surface mapping and localize spot positions in latitude and longitude. With forthcoming high-precision Gaia astrometry, astrometric surface mapping provides a promising new approach to probe stellar activity.

### 1. INTRODUCTION

In a star-planet system, each body orbits the mutual center of mass; this is called reflex motion. By precisely measuring the star's orbital reflex motion, astrometry has thus far been used to detect and estimate the masses of large exoplanets and companion stars (G. Stefánsson et al. 2025). Detecting Earth-mass planets in the habitable zones of Sun-like stars, however, requires sub-microarcsecond sensitivity (0.3  $\mu$ as for an Earth-Sun analog) (M. Perryman 2018). Achieving sub-microarcsecond astrometric precision is the most promising route to mass determination of an Earth analogue, as, compared to the main alternative, radial velocity (RV), the expected signal-to-noise is an order of magnitude less impacted by stellar variability (V. V. Makarov et al. 2009). Unlike detecting transit signatures, where the geometric likelihood of a planet transit falls off with the planets semi-major axis, an exoplanets astrometric signal strength  $\alpha$  increases with semi-major axis:  $\alpha \propto \frac{M_p}{M_*} \frac{a}{D}$ , where  $\frac{M_p}{M_*}$  is the planet-to-star mass ratio,  $a$  is the planets semi-major axis and  $D$  is distance (M. Shao et al. 2009). Furthermore, astrometry obtains true mass estimates

Corresponding author: Jamila Taaki  
 xiaziyna@gmail.com

liac@umich.edu

hero@eecs.umich.edu

because it fits the sky plane orbit, unlike RV, which yields only a minimum exoplanet mass  $M_p \sin(i)$  as the orbital inclination  $i$  is unknown (J. Wright & B. Gaudi 2012). Diffractive pupil astrometry (O. Guyon et al. 2011) has been proposed as a method to achieve sub-microarcsecond astrometric precision, and lab demonstrations have shown feasibility (E. A. Bendek et al. 2013). This technique uses diffraction spikes to calibrate deformations in the optical field and obtain relative astrometry from background stars. Proposed diffractive-pupil missions include TOLIMAN (E. Bendek et al. 2021) to search for planets around Alpha Centauri, SHERA (J. Christiansen 2025), and integrated coronagraph-astrometry telescopes (O. Guyon et al. 2012). Once sub-microarcsecond astrometric precision is reached, starspot noise is the major limiting factor in detecting and measuring exoplanets.

Starspots caused by magnetic activity can cause significant shifts in the photo-center of the star, termed *astrometric jitter*, that can obscure true reflex motion (V. V. Makarov et al. 2010). Astrometric jitter poses a significant challenge for measuring Solar-system analogs, and mitigating starspot noise has been identified as a key area for future astrometry and RV missions (K. Stapelfeldt & E. Mamajek 2025). In this work, we show that the astrometric jitter of a rotating star encodes surface-brightness information that can be used to map stellar surfaces and help constrain starspot features. While light curves have been previously used to map stellar surfaces H. N. Russell (1906); R. Harmon & L. Crews (2000); R. M. Roettenbacher et al. (2017); N. B. Cowan et al. (2013a); H. M. Haggard & N. B. Cowan (2018); R. Luger et al. (2021b,a), astrometry probes complementary surface information and can better localize the positions of starspots on stellar surfaces. In principle, a joint astrometric fit could recover both the stellar surface and the true stellar reflex motion.

Starspots form where regions of strong magnetic flux suppress convection, producing cooler, darker regions on the photosphere (S. Solanki 2003). While solar-like levels of starspot coverage, some 0.03 – 0.05% of the visible stellar surface at solar maximum (B. M. Morris et al. 2018), have limited impact on astrometric mass measurement precision (J. Catanzarite et al. 2008; V. V. Makarov et al. 2010; Eriksson, U. & Lindegren, L. 2007), younger, more active or rapidly rotating stars may far exceed the Sun’s 0.5  $\mu$ as level of jitter at 10 pc, posing a major challenge for mass determination (A. I. Shapiro et al. 2021; F. Nichols-Fleming & E. G. Blackman 2019). In particular, M dwarfs often host large spot complexes that can remain stable over many rotations. For example, the M-dwarf TOI-3884 shows a polar spot with a possible  $\approx 0.44R_\star$  radius (J. M. Almenara et al. 2022). N. Meunier & A. M. Lagrange (2022) show that the detection of exoplanets with longer orbital periods around nearby stars will be most impacted by astrometric jitter. Furthermore, even for the best F G K candidate stars, Earth-mass uncertainties due to starspot jitter are expected to be some 30% on average (N. Meunier & A. M. Lagrange 2022). C. Bao et al. (2024) utilize a single-starspot model from B. M. Morris et al. (2018) and simulated astrometric jitter for 78 solar-like *TESS* targets, similarly finding some 30% mass uncertainty for Earth-mass planets at 10 pc. M. Damiano et al. (2025) find a mass uncertainty below 10 % is needed to identify atmospheric compositions of Earth analogues. Future missions to characterize Earth analogues, e.g., the Habitable Worlds Observatory (HWO), may also rely on planets found through astrometry. Thus, characterizing the impact of stellar signatures on astrometric measurements remains an important problem.

The Gaia mission is set to deliver two successive data releases (DR4 and DR5, the end-of-mission release) of ultra-precise astrometric measurements for over two billion stars ( Gaia Collaboration et al. 2016). With forthcoming Gaia data releases, the sensitivity required to map starspots with astrometry will soon be reached. Our work lays out the methods to do this. B. M. Morris et al. (2018) use an analytic spot model to show nearby ( $< 5$  pc) low-mass stars are excellent candidates for detecting spot-induced jitter with Gaia. Additionally, K. Sowmya et al. (2022) models solar-like stars rotating faster than the sun, producing higher levels of magnetic activity, and shows that their star spot coverage is detectable with Gaia. Over its 55-month mission, Gaia will achieve  $\sim 7$   $\mu$ as precision for the Gaia magnitude  $G < 12$  targets. For the brightest  $G \sim 5 - 8$  mag nearby targets studied in B. M. Morris et al. (2018), end-of-mission precisions in position/parallax of the order of 3 – 5  $\mu$ as are estimated after stacking  $\sim 100$  visits. In anticipation of these data releases, we develop astrometric surface mapping techniques to apply to these targets. Although motivated by the need to understand starspot features and mitigate stellar jitter in astrometric surveys, more broadly, this work provides a new way to map starspots and stellar surfaces.

While Doppler imaging (S. S. Vogt et al. 1987), and interferometry (J. D. Monnier et al. 2007; M. Zhao et al. 2009; R. M. Roettenbacher et al. 2017; J. R. Parks et al. 2021) have been used to map a handful of large, partially resolved, nearby stars, stellar surface mapping has primarily been performed using light curves, both through transit-eclipse mapping (A. V. R. Silva 2003) and rotational light-curve mapping (H. N. Russell 1906). Light curve, or photometric, mapping uses the disc-integrated flux over time to map a stellar surface. As noted by R. Luger et al. (2021b), the Kepler and *TESS* space telescopes, with their extreme levels of photometric sensitivity, have enabled the ensemble

properties of large numbers of stars to be studied. However, light-curve inversion is fundamentally ill-posed since one seeks to reconstruct a high-dimensional surface map from low-dimensional disc-integrated flux measurements, and a unique surface map solution does not exist (L. M. Walkowicz et al. 2013; G. Basri & R. Shah 2020). Interferometric imaging may carry more information about a stellar surface depending on the array’s baseline geometry. S. Dholakia & B. J. S. Pope (2025) derives analytic expressions for the interferometric visibility function response to surface spherical harmonics at a fixed stellar inclination. R. M. Roettenbacher et al. (2017) provide a direct comparison of fitting a spot model to  $\sigma$  Gem with interferometric, Doppler, and light-curve data. All three techniques reproduce the longitudinal spot distribution. However, light-curve inversion cannot reliably recover spot latitudes, and Doppler imaging also shows latitude biases. By obtaining complementary measurements, our work demonstrates that astrometry can break light curve inversion degeneracy and improve the accuracy of stellar surface maps.

H. N. Russell (1906) introduced spherical harmonics as a tool to characterize the retrievable information in the light curve of a rotating star. A pixelized basis of the stellar surface has also been used (R. Harmon & L. Crews 2000). Furthermore, analytic spot-based light-curve models have been described (J. D. Dorren 1987; D. M. Kipping 2012). Spherical harmonics provide a complete orthogonal representation of any spherical surface, with higher degrees capturing progressively finer spatial structure. Working in this coordinate space H. N. Russell (1906); N. B. Cowan et al. (2013b,a) have derived semi-analytic expressions of disc-integrated flux (light-curve) of a rotating body over time, which are additionally used for mapping exoplanets (E. Rauscher et al. 2018). R. Luger et al. (2021b) and N. B. Cowan et al. (2013b) both characterize the degeneracy of rotational light-curve inversion, showing that odd-degree spherical harmonics are in the null-space of the light curve measurement operator and thus are not measurable with photometry. Our work shows that astrometry does measure odd-degree spherical harmonics, completing the sampling of the spherical-harmonic basis and obtaining additional information about the stellar surface.

In this work, we explore stellar surface inversion with astrometric measurements. We derive an analytic, linear, forward model that describes the rotational astrometric signal generated by an arbitrary stellar surface at any inclination. To derive the forward model, we obtain analytic expressions for the photo-centre in terms of spherical-harmonic coefficients representing the stellar surface. Because the spherical harmonic basis is naturally ordered by spatial scale, it can be truncated at a degree set by the measurement sensitivity and the resulting spatial resolution, reducing the infinite-dimensional inversion problem to a finite-dimensional subspace. Wigner-D rotation matrices are used to obtain rotations of the stellar surface; these are semi-analytical, linear expressions for rotations in the spherical harmonic basis. Building on this, we characterize the degradation in the stellar surface information and develop a surface inversion approach. We perform proof-of-concept reconstructions of simulated stellar surfaces and demonstrate improved ability to recover stellar inclination and localize star-spot features by combining astrometry and photometry.

This paper is organized as follows. Section 2 describes the forward astrometric model of a rotating stellar surface under a spherical harmonic decomposition. Section 3 describes the astrophysical implications of surface mapping with photometry and astrometry, and conclusions are presented in Section 4.

## 2. METHODS

We can describe the image of a stellar surface as a linear combination of spherical harmonics, so that the astrometric time series becomes a linear function of these stellar surface weightings. This linear forward model allows us to treat surface mapping geometrically using vector-space theory. In this framework, a measured astrometric signal can be obtained by a well-defined subspace of spherical surfaces. Within this solution space, priors or regularisation can be used to choose a unique surface solution. The vector space approach to inverse problems is commonly used in signal and image processing, see Y. Bresler et al. (2000) for more details on the techniques used here. We assume a non-time-varying static surface without differential rotation. Dynamically evolving surfaces and limb darkening are left for future work.

Uppercase symbols denote matrices (e.g.,  $A$ ), bold lowercase symbols denote column vectors (e.g.,  $\mathbf{s}$ ), and non-bolded lowercase symbols are generally scalars or functions (e.g.,  $s$ ). We denote the conjugate transpose of a matrix or vector  $A$  by  $A^H = (A^*)^T$  and the complex conjugate of a scalar as  $s^*$ . Notation is provided in Table 1.

Let the stellar surface brightness map of a star be defined in spherical coordinates as  $s(\theta, \phi) \in \mathcal{R}$ , defined for spherical polar angle  $\theta \in [0, \pi]$  and azimuthal angle  $\phi \in [-\pi, \pi]$ . Spherical harmonics provide a complete, orthonormal basis for any spherical surface, and can therefore exactly represent any stellar surface  $s(\theta, \phi)$ . By expanding the stellar surface  $s(\theta, \phi)$  as a linear combination of harmonics, with higher degrees capturing progressively finer structure, we

**Table 1.** Table of notation

Symbol	Type	Meaning
$h \in \{x, y\}$	index	Measurement axis (observer-frame).
$l, m$	indices	Spherical-harmonic degree ( $l = 0, \dots, L$ ) order ( $m = -l, \dots, l$ ).
$Y_l^m(\theta, \phi)$	function	Complex spherical harmonic.
$\mathbf{s} \in \mathcal{C}^{(L+1)^2}$	vector	Stellar surface coefficients $[s_0^0, \dots, s_l^m, \dots, s_L^L]^T$ .
$R = (\alpha, \beta, \gamma)$	spherical angle	Euler angles ( $z - y - z$ ); $\beta$ is stellar inclination, $\gamma = \omega t$ where $\omega$ is stellar rotation rate.
$D^l(R)$	matrix	Wigner- $D$ rotation (for $R$ ) matrix for spherical harmonic coefficients
$k_{lm}^h$	scalar	First-moment (astrometric) kernel for $(l, m)$ along measurement axis $h$ .
$\mathbf{k}_l^h \in \mathcal{C}^{2l+1}$	vector	Degree- $l$ kernel over $m$ for axis $h$ .
$B_\beta^h \in \mathcal{C}^{(2L+1) \times (L+1)^2}$	matrix	Inclination dependent matrix in forward model.
$W_\omega \in \mathcal{C}^{N \times (2L+1)}$	matrix	Time dependent matrix for $N$ observation times, $[W_\omega]_{n,m} = e^{-im\omega t_n}$ .
$A(\beta) \in \mathcal{C}^{2N \times (L+1)^2}$	matrix	Astrometric measurement matrix (applied to $\mathbf{s}$ ).
$\boldsymbol{\mu} \in \mathcal{C}^{2N}$	vector	$A_{1:N}(\beta) = W_\omega B_\beta^x, A_{N+1:2N}(\beta) = W_\omega B_\beta^y$
$\mathbf{n} \sim \mathcal{N}(\mathbf{0}, \sigma^2 I)$	vector	Stacked measurement $[\boldsymbol{\mu}^x, \boldsymbol{\mu}^y]^T = A(\beta)\mathbf{s}$ .
$\mathbf{y}$	vector	Measurement noise with variance $\sigma^2$ .
		Noisy measurements, $\mathbf{y} = \boldsymbol{\mu} + \mathbf{n}$ .

can analytically characterize the rotational astrometric signal contributed by each harmonic term individually. Using these expressions, we can map an arbitrary star's surface coefficients to the measured astrometric jitter signal.

We define the complex spherical harmonics basis set:

$$Y_l^m(\theta, \phi) = N_l^m P_l^m(\cos \theta) e^{im\phi}, \quad (1)$$

indexed by degree  $l = 0, 1, \dots, L$ ,  $m = -l, \dots, l$ , where  $P_l^m$  are the Legendre polynomials and  $N_l^m$  is a constant. The spherical stellar surface can be approximated to arbitrary accuracy by its spherical harmonic expansion in this basis up to a degree  $L$  as a vector of coefficients  $\mathbf{s} \in \mathcal{C}^{(L+1)^2}$ . As the maximum degree is allowed to go to infinity  $L \rightarrow \infty$ , the approximation becomes exact.

$$s(\theta, \phi) = \sum_{l=0}^L \sum_{m=-l}^l s_l^m Y_l^m(\theta, \phi) \quad (2)$$

Where  $s_l^m = \int_0^{2\pi} \int_{-\pi/2}^{\pi/2} s(\theta, \phi) Y_l^m(\theta, \phi) \sin(\theta) d\theta d\phi$ . The spherical harmonic representation of the stellar surface is then given by  $\mathbf{s} = [s_0^0, s_1^{-1}, s_1^0, \dots]^T$ . For computation, we truncate the sum in Equation 2 to a finite value  $L$ . Because the astrometric sensitivity declines with increasing  $l$ , the maximum degree  $L$  is chosen to match the effective noise floor. This sensitivity structure is described in Section 2.2.

We use the complex spherical-harmonic basis for algebraic convenience when applying rotations, but the physical surface is modeled as real by enforcing the constraint on  $\mathbf{s}$  that  $s_l^{-m} = (-1)^m (s_l^m)^*$ ,  $s_l^0 \in \mathcal{R}$  where  $s^*$  is the complex conjugate of  $s$ . This constraint reduces the effective degrees of freedom by half (for  $m > 0$ ) and means the rotated surface measurements are also real.

Astrometric measurements obtain the centroid of the star, i.e., the first moment of the star normalized by the zeroth moment (disc-integrated flux) at each timestep. This is a non-linear function of the stellar surface. We consider the first moment alone, as it can be directly obtained from the instrument, and we refer to this as the astrometric signal. The astrometric operator measures the first moment of the visible hemisphere at a point in time, as projected onto the observer's 2D x-y plane. We take the observer to lie along the 3D x-axis of the spherical frame. The astrometric measurement operators are  $\mathcal{A}_x : L^1(S^2) \rightarrow \mathcal{R}$  and  $\mathcal{A}_y : L^1(S^2) \rightarrow \mathcal{R}$  and are given in Appendix B, where  $L^1(S^2)$  denotes the class of integrable functions defined on the unit sphere and  $\mathcal{R}$  denotes the real numbers.

We use Euler angles  $R = (\alpha, \beta, \gamma)$  to describe the rotation of the star about an inclined axis. Rotations are applied left to right:  $\alpha$  first, followed by  $\beta$  and  $\gamma$ . Here  $\alpha$  is the sky-plane tilt and assumed to be zero.  $\beta \in [0, \pi/2]$  is the inclination of the rotational axis; when  $\beta = 0$ , the observer faces the equator of the star, when  $\beta = \pi/2$  the observer

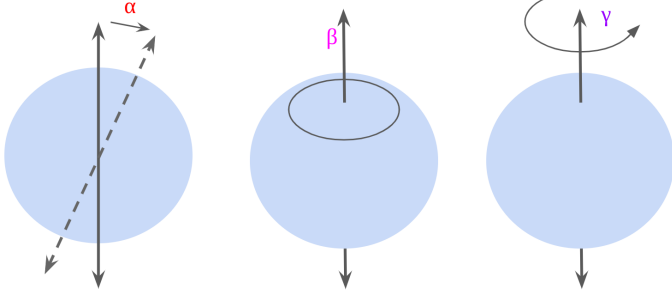


**Figure 1.** Stellar rotation geometry (applied right to left). We parameterise the orientation with Euler angles  $R = (\alpha, \beta, \gamma)$  in the  $z - y - z$  convention, mapping the star-fixed frame to the sky via  $R = R_z(\alpha)R_y(\beta)R_z(\gamma)$ . Here  $\beta$  is the inclination (tilt) of the spin axis,  $\gamma = \omega t$  is the time-dependent rotation at angular rate  $\omega$ , and  $\alpha$  sets the sky-plane tilt.

faces the pole. The time-dependent spin is  $\gamma = \omega t$  with rotation rate  $\omega = \frac{2\pi}{P}$  where  $P$  is the rotation period of the star. We can represent rotations of the star directly within the spherical harmonic basis. Rotations on the sphere in the spherical harmonic basis are described by Wigner D rotations (J. J. Sakurai & J. Napolitano 2020), transforming the coefficient vector  $\mathbf{s}_l$  for each degree  $l$  as  $\mathbf{s}'_l = D^l(R)\mathbf{s}_l$ , where  $D^l(R)$  is the Wigner D-matrix corresponding to rotation  $R$ . This enables efficient rotation of the coefficient representations without direct rotations of the surfaces. The forward model of degree  $L$  then describes the first moment  $\mu^h(R) : h \in \{x, y\}$  of the stellar surface after applying a rotation  $R$ :

$$\mu^h(R) = \mathcal{A}_h \left( \sum_{l \geq 0}^L \sum_{m=-l}^l [D^l(R)\mathbf{s}_l]_m Y_l^m(\theta, \phi) \right). \quad (3)$$

Since the astrometric operator  $\mathcal{A}_h$  is a first-moment integral (defined in Appendix B), it is a linear operator. When this linear operator is applied to a linear summation of spherical harmonics with scalar weights  $[D^l(R)\mathbf{s}_l]_m$ , we can equivalently take the summation of the astrometric operator applied to each static unrotated spherical harmonic as  $\mathcal{A}_h(Y_l^m(\theta, \phi))$ . We refer to these responses as the astrometric kernel, since they encode the sensitivity of the photocentre to individual spherical-harmonic modes.

The astrometric operator applied to spherical harmonics produces complex-valued astrometric kernel terms  $k_{l,m}^h = \mathcal{A}_h(Y_l^m(\theta, \phi)) \in \mathcal{C}$ , or  $\mathbf{k}^h$  in vector form. This astrometric kernel is described in detail below in Section 2.2. We can rewrite Equation A1 with the astrometric kernel as:

$$\mu^h(R) = \sum_{l=0}^L \sum_{m=-l}^l [D^l(R)\mathbf{s}_l]_m k_{l,m}^h. \quad (4)$$

Next, we note that Equation 4 is an inner product between  $\mathbf{k}_l^h$ , the degree  $l$  kernel terms, and the rotated surface coefficients  $\mathbf{s}_l$ . Writing the astrometric signal as an inner product, and by further utilizing the conjugate symmetry of the inner product, we obtain:

$$\mu^h(R) = \sum_{l=0}^L \langle D^l(R)\mathbf{s}_l, \mathbf{k}_l^h \rangle = \sum_l \langle \mathbf{s}_l, D^{l,H}(R)\mathbf{k}_l^h \rangle, \quad (5)$$

where  $D^{l,H}(R)$  is the conjugate transpose of the rotation. Because a rotation matrix is unitary, the conjugate transpose is the same as inverting the rotation, so that

$$D^{l,H}(\alpha, \beta, \gamma) = D^l(-\gamma, -\beta, -\alpha). \quad (6)$$

In this form, the astrometric measurement is given by an inner product between  $\mathbf{s}$  and the rotated kernel terms. The full forward model is a time series of photocentre measurements produced by rotating these kernel terms at different times (equivalently rotations  $R = (0, \beta, \omega t)$ ) with the analytic Wigner-D matrices. This yields a matrix formulation

that can be applied to any stellar surface. By decomposing this matrix into time-dependent and inclination-dependent factors, and inspecting how rotations mix the kernel terms (and, in parallel, the photometric kernel), we can cleanly characterize the information content of astrometry and photometry side by side. Below, we summarize the time-series forward model and detail the structure of the astrometric kernel to obtain our key insight that astrometry and photometry obtain distinct information about stellar surfaces.

### 2.1. Time and inclination separable forward model

For  $N$  astrometric observations at times  $t_1, \dots, t_N$  and  $h \in \{x, y\}$ , we define the astrometric time series  $\mu^h$  as:

$$\mu^h = [\mu^h(R_{t_1}), \dots, \mu^h(R_{t_N})]^T. \quad (7)$$

In Appendix A, a compact forward model for  $\mu^h$  is derived using Equation 5. In this form, the forward model is independent of the specific surface realization  $\mathbf{s}$ , allowing us to precompute the measurement matrix based solely on observational parameters such as the inclination  $\beta$ , spin rate  $\omega$ , and measurement times of the following form:

$$\mu^h = W_\omega B_\beta^h \mathbf{s}. \quad (8)$$

We stack the first moment time series in  $x$  and  $y$  and call the following description of the astrometric signal  $\mu$  the forward model:

$$\mu = \begin{bmatrix} \mu^x \\ \mu^y \end{bmatrix} = A(\beta) \mathbf{s}, \quad A(\beta) = \begin{bmatrix} W_\omega & B_\beta^x \\ & W_\omega \end{bmatrix} \begin{bmatrix} B_\beta^x \\ B_\beta^y \end{bmatrix}. \quad (9)$$

The signal matrix  $A(\beta)$  that acts on  $\mathbf{s}$  encapsulates the time-dependent mapping from the visible surface to photocentre measurements. In this form, the forward model consists of a time-dependent matrix  $W_\omega \in \mathcal{C}^{N \times (2L+1)}$  and an inclination dependent matrix  $B_\beta^h \in \mathcal{C}^{(2L+1) \times (L^2+1)}$ ,  $B_\beta^h$  further depends on kernel terms  $\mathbf{k}^x$  or  $\mathbf{k}^y$ , these can be swapped out for the photometry kernel without changing the other components of the forward model. This forward model describes observations for any inclination  $\beta \in [0, \pi/2]$ .  $W_\omega$  can be calculated for arbitrary observation times. We assume there are at least  $2L + 1$  uniform measurement times over the star's rotation period. This yields a  $W_\omega$  that is unitary (information preserving), where the  $m^{\text{th}}$  column of the matrix corresponds to a complex sinusoid of frequency  $m\omega$  evaluated at times  $\{t_1, \dots, t_N\}$  over a single rotation. In other words,  $W_\omega$  behaves like an inverse Fourier transform matrix by synthesizing together complex sinusoids weighted by the  $m^{\text{th}}$  row of  $B_\beta \mathbf{s}$ . This decoupling of the spin (via  $W_\omega$ ) and inclination (via  $B_\beta^h$ ) in the forward model provides key benefits for analytical insight and computational efficiency in the inverse problem of stellar surface reconstruction. Analytically, it isolates the impact of inclination on the model rank, making it simple to analyse how the surface solution set changes with inclination. Figure 2 shows the variation in the astrometric signal of a simulated star with a starspot over a full rotation for different inclinations. Figure 3 shows the astrometric signal at a fixed inclination for starspots at various latitudes. In Section 2.2, we describe the complementarity of the astrometric and photometric kernels, and in Section 2.3, we describe the surface information content of astrometric jitter.

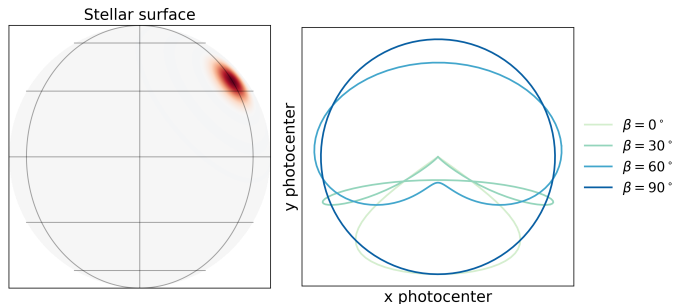


**Figure 2.** An order  $L = 25$  expansion of an  $8\% R_\star$  starspot. The star surface is shown (left) viewed equatorially. The astrometric signal is shown for different inclinations ranging from  $\beta = 0$  (equator on) to  $\beta = \pi/2$  (pole down). When the photo-center is at origin, the starspot is out of view. For a pole-down observer, any astrometric signal is circularized.

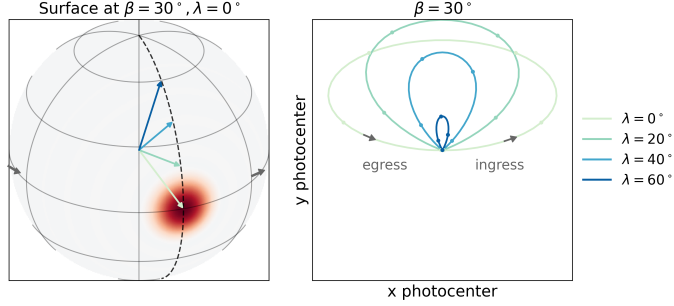


**Figure 3.** An order  $L = 25$  expansion of a 10 %  $R_\star$  starspot. The star surface is shown (left) at an inclination of  $\beta = 30^\circ$ , with an equatorial starspot. For this stellar inclination, the astrometric signal from starspots at different latitudes denoted by  $\lambda$  is shown (right), ranging from  $\lambda = 0^\circ$  (equatorial) to  $\lambda = 60^\circ$ . Grey arrows denote the egress and ingress of the starspot. As the starspot heads to egress, the photocenter moves toward the origin. While the starspot is out of view, the photocenter is fixed at zero. When the starspot moves into ingress, the photocenter begins to move again. These varying starspot latitudes  $\lambda$  are shown on the stellar surface (right) as arrows pointing from the star's interior origin point. Furthermore, starspots at higher latitudes generally produce less photo-center variation.

## 2.2. Astrometry measures odd degree $l$ harmonics

Above, we summarized the forward model that maps a stellar surface in spherical harmonics to an astrometric time series. This forward model depends on kernel terms  $k_{l,m}^h$  :  $h \in \{x, y\}$ , which describe the astrometric sensitivity to individual spherical harmonics of degree  $l$  and order  $m$ . In this section, we describe the kernel form and how stellar inclination affects this sensitivity. Later, in Section 2.3, we discuss the inversion degeneracy.

In a static unrotated frame, the kernel terms describe the photo-center of each spherical harmonic  $k_{l,m}^h = \mathcal{A}_h(Y_l^m(\theta, \phi))$ . For our chosen convention, the astrometric kernel terms  $\mathbf{k}^h$  :  $h \in \{x, y\}$  are defined for an observer along the 3D x-axis (in the spherical frame), as projected onto their 2D x-y plane of the sky (the x-y observer axis correspond to the y-z axis in the spherical frame). These kernel terms are derived as analytic integrals in Appendix B, where we identify spherical harmonics that produce zero-valued kernel terms using the symmetry properties of the functions being integrated.

A key analytic result of this work is that astrometry measures odd  $l$  spherical harmonics that are anti-symmetric about the equator, in contrast to photometry, which measures even  $l$  degree harmonics that are symmetric about the equator (N. B. Cowan et al. 2013a). Astrometry and photometry, therefore, probe orthogonal subspaces of the stellar surface, meaning that joint astrometry–photometry measurements can recover surface structure inaccessible to either measurement type alone. For astrometry, the kernel terms are non-zero for odd  $l$  and  $l = 2$ , and the x-direction kernel is non-zero for harmonics of odd order  $m > 2$ , while the y-direction kernel is non-zero for harmonics of even order  $m > 2$ . For these non-zero cases, the kernel weights are integrals over the Legendre polynomials  $P_l^m(\eta)$  given by:

$$k_{l,m}^x = \begin{cases} \frac{I_{\phi,x}(m)N_l^m}{\pi} \int_{-1}^1 (1 - \eta^2) P_l^m(\eta) d\eta & \text{if } (l \text{ odd and } m \text{ odd}) \text{ or } (l = 2 \text{ and } |m| = 2), \\ 0 & \text{otherwise,} \end{cases} \quad (10)$$

$$k_{l,m}^y = \begin{cases} \frac{I_{\phi,y}(m)N_l^m}{\pi} \int_{-1}^1 \eta \sqrt{1 - \eta^2} P_l^m(\eta) d\eta & \text{if } (l \text{ odd and } m \text{ even}) \text{ or } (l = 2 \text{ and } |m| = 1), \\ 0 & \text{otherwise.} \end{cases}$$

Where  $\eta$  is the variable of integration and  $I_{\phi,h}(m)$  terms are given in Appendix B. We evaluate the inner integral numerically using Sympy (A. Meurer et al. 2017), achieving a relative error of order  $\sim 10^{-15}$ . The kernel terms need only be evaluated once and can be used to derive the rotational signatures for different stars or different inclinations. These are shown evaluated up to  $L = 7$  for an equatorial  $\beta = 0$  stellar inclination in Figure 4 and mid-inclination in Figure 5, alongside the photometry kernel derived by N. B. Cowan et al. (2013a). Intuitively, the pattern shown in this Figure arises because the astrometric operator measures the visible centroid, which integrates an antisymmetric position weighting multiplied by the visible surface. Hence, this will only be non-zero if the visible surface is asymmetric.

For an equatorial observer ( $\beta = 0$ ), the astrometric kernel exactly describes the relative weighting of spherical harmonics to the astrometric signal because the Wigner-D matrix in Equation 5 is an identity matrix. The kernel terms in Equation 10 illustrate that astrometric measurements of a star viewed equatorially ( $\beta = 0$ ) probe independent spherical harmonics; the  $x$  direction probes odd-order harmonics, while the  $y$  direction probes even-order harmonics. However, when a star is inclined, the kernel terms for each degree  $l$  are mixed among orders  $m \in \{-l \dots l\}$  within each  $l$  as  $(\mathbf{k}_l^h)' = C_\beta^l \mathbf{k}_l^h$ , where  $C_\beta^l$  is an inclination dependent Wigner-D matrix. The matrix  $B_\beta^h$ , which is derived in Appendix A, captures this and is visualized in Figure 5. Because mixing is applied separately per degree  $l$ , even degrees  $l > 2$  with zero-valued kernel terms remain zero after mixing and are unobservable. Likewise, for photometry, odd-degree harmonics remain unobservable. Consequently, astrometry and photometry remain complementary when the star is inclined.

However, as described in N. B. Cowan et al. (2013b), because of this mixing by  $C_\beta^l$ , for an odd-degree  $l$ , all order  $m$  reweighted kernel terms in the vector  $(\mathbf{k}_l^h)'$  are non-zero. Thus, the corresponding spherical harmonics are observable when the star is at an interior inclination  $\beta \in (0, \pi/2)$ . As a result, a larger number of spherical harmonics contribute to the astrometric or photometric signal when the star is inclined, and we retrieve more information about the stellar surface. We discuss the implications of this result for mapping the surface below in Section 2.3.

As can also be seen in Figures 4 and 5, the individual coefficients  $k_{l,m}^h$  decrease in magnitude with increasing degree  $l$ . This diminishing sensitivity allows us to truncate the spherical harmonic representation at a maximum degree  $L$  while maintaining a desired level of accuracy. However, this does not necessarily imply that higher-degree terms are negligible in the total observed signal. Each degree  $l$  contains  $2l + 1$  spherical harmonic modes, so the aggregate contribution of terms above a given degree  $l$  depends on the rate of decay of  $|k_{l,m}^h|$  and the growing number of modes. In other words, even if each coefficient becomes small, the sum over all degrees and orders may be a significant factor in the spherical harmonic approximation.

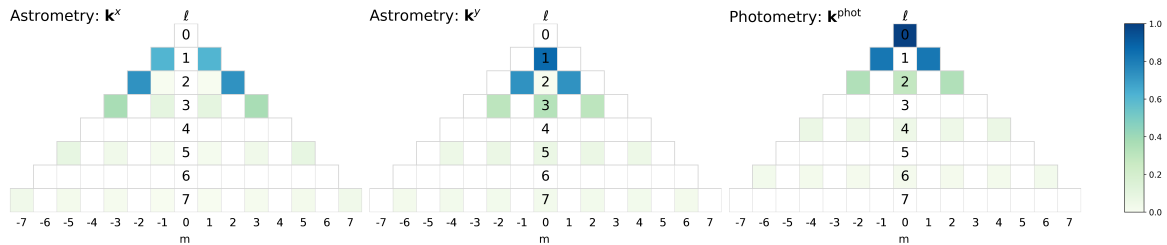


**Figure 4.** Visualizing the measurement kernels  $\mathbf{k}$  for the first-order moments (astrometry) and zeroth-order moments (light curve photometry) over the spherical harmonic basis indexed by  $(l, m)$ . For a star viewed equatorially, where the kernel is 0 (white) for the  $(l, m)$  harmonic, this harmonic term produces no measurable signal. The magnitude of each kernel term is the contribution to the astrometric signal for that particular spherical harmonic, in other words how strongly that spherical harmonic component shifts the photocenter. The astrometry operator follows a pattern where even-valued  $l > 2$  cannot be measured, whereas the photometry operator follows the opposite pattern, odd-valued  $l > 2$  cannot be measured. Therefore, astrometry obtains complementary information to light curve data, and combined, can better constrain a stellar surface estimate.

For the edge cases of inclinations  $\beta = 0$  (equator on) and  $\beta = \pi/2$  (pole down), we obtain no mixing of the kernel terms. For the polar observer, all but the  $m = \pm 1$  harmonics are weighted to zero. Below, we summarize the astrometric signal induced by individual spherical harmonics  $Y_l^m(\theta, \phi)$  for these edge-case stellar inclinations.

*Rotating star viewed equatorially:  $\beta = 0$* —In the equatorial case, the astrometric kernel terms  $\mathbf{k}^h$  directly weight complex exponential oscillation terms, we obtain the following astrometric measurements for the stellar surface harmonics:

$$\mu_{l,m}^x(t) = \begin{cases} e^{im\omega t} k_{l,m}^x & \text{if } (l \text{ odd and } m \text{ odd}) \text{ or } (l = 2 \text{ and } |m| = 2), \\ 0 & \text{otherwise,} \end{cases} \quad (11)$$

$$\mu_{l,m}^y(t) = \begin{cases} e^{im\omega t} k_{l,m}^y & \text{if } (l \text{ odd and } m \text{ even}) \text{ or } (l = 2 \text{ and } |m| = 1), \\ 0 & \text{otherwise,} \end{cases} \quad (12)$$

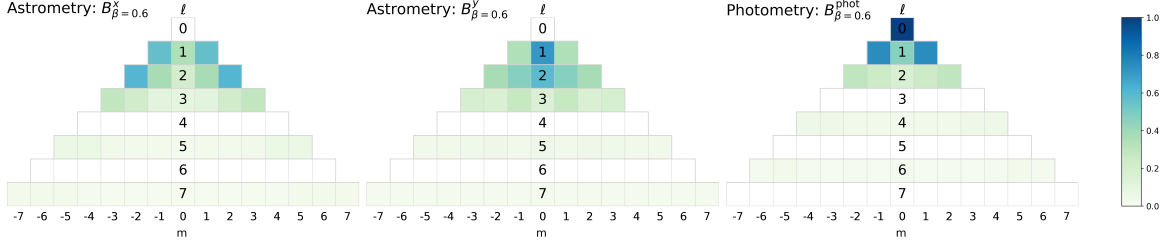


**Figure 5.** Visualizing the observable spherical harmonics and their weightings when the star is inclined by  $\beta = 0.6$ . The inclination dependent matrix in the forward model,  $B_\beta$  comprises diagonal sub-matrices where the inclination rotation is applied to each of the kernel terms  $\mathbf{k}_l^h$ . Here we show these values over the spherical harmonic basis indexed by  $(l, m)$ . Where the kernel is 0 (white) for the  $(l, m)$  harmonic, this harmonic term does not contribute to the measured signal. For an inclined star, the kernel terms  $\mathbf{k}_l^h$  have been ‘mixed’ over order  $m$  per degree  $l$ , rendering unobservable terms observable and doubling the overall rank of the forward model. All odd degree  $l$  harmonics now contribute to the observations in both astrometric directions, and all even degree  $l$  harmonics contribute to the photometric observations. As shown, when a star’s rotational axis is inclined, astrometry and photometry still generally obtain measurements from distinct collections of spherical harmonics.

*Rotating star viewed from the pole:  $\beta = \pi/2$* —This case is the most ill-conditioned and rank-deficient. For any stellar surface, the signal is purely circular. Equivalently, the astrometric harmonics are non-zero only for  $|m| = 1$ . The terms  $p_{l,m}^h$  are weightings defined in Appendix B.3

$$\mu_{l,m}^x(t) = \begin{cases} e^{im\omega t} p_{l,m}^x & \text{if } (l \text{ odd or } l = 2) \text{ and } |m| = 1 \\ 0 & \text{otherwise,} \end{cases} \quad (13)$$

$$\mu_{l,m}^y(t) = \begin{cases} e^{im\omega t} p_{l,m}^y & \text{if } (l \text{ odd or } l = 2) \text{ and } |m| = 1 \\ 0 & \text{otherwise,} \end{cases} \quad (14)$$

Finally, since the observed first moment is found as the sum over the contributions in  $l, m$ , for a stellar surface described by coefficients  $s_l^m$ , the overall astrometric signal is given by:

$$\mu^x(t) = \mu^y(t) \propto e^{i\omega t} \sum_{\text{odd } l} (s_l^1 + s_l^{-1}). \quad (15)$$

Although this is the most weakly constrained case for inversion, it can also produce the strongest signal as the rotated kernel weightings  $p_{l,m}^h$  are large and produce equal displacements in both  $x$  and  $y$  directions. Consistent behaviour is seen by K. Sowmya et al. (2021), showing pole-on configurations produce significant astrometric jitter that can interfere with measurements of planetary reflex motion.

### 2.3. Astrometric inversion degeneracy

#### 2.3.1. Rank and nullity

Although many spherical harmonics can produce non-zero astrometric signals, subsets of these observable harmonics can produce indistinguishable time series, making the inversion degenerate. The row-space and its complement, the null-space of the astrometric operator  $A(\beta)$ , characterize the space of possible stellar surface solutions  $\mathbf{s}$  for noiseless measurements  $\boldsymbol{\mu}$  and how this varies with inclination angle  $\beta$ . The null-space denoted as  $N(A(\beta))$  consists of all surfaces  $\mathbf{s} \in N(A(\beta))$  such that  $A(\beta)\mathbf{s} = 0$ , meaning these components produce no detectable astrometric motion in  $x$  or  $y$  and are thus inherently unobservable. Conversely, the row space of  $A(\beta)$  describes all stellar surface coefficient vectors  $\mathbf{s}$  that produce non-zero measurements and have no component lying in the null space. The row space is the orthogonal complement of the null-space  $\text{Row}(A(\beta)) = N(A(\beta))^\perp$ , thus any surface can be uniquely decomposed into a combination of a row space vector and a null space vector.

$$\mathbf{s} = \mathbf{s}_{\text{Row}(A)} + \mathbf{s}_{N(A)}$$

If a particular surface  $\mathbf{s}_{\text{Row}(A)}$  produces an astrometric signal  $\boldsymbol{\mu}$ , then any additive surface drawn from the null space  $\mathbf{s}_{N(A)}$  leaves the astrometric signal unchanged:

$$A(\beta)\mathbf{s}_{\text{Row}(A)} = \boldsymbol{\mu} \Rightarrow A(\beta)(\mathbf{s}_{\text{Row}(A)} + \mathbf{s}_{N(A)}) = \boldsymbol{\mu} \quad \text{for all } \mathbf{s}_{N(A)} \in N(A(\beta)).$$

Given an astrometric signal  $\mu$ , solving for a surface  $\mathbf{s}$  is unique only up to the row space. The size of the null space characterizes the bias in estimating a stellar surface from measurements. If the null space spans all spherical harmonics, it would mean we could not identify any surface solution. If the null space is empty, we can uniquely constrain the stellar surface from the measurements. The dimension of the null space is denoted as  $\text{nullity}(A(\beta))$  and is thus a measure of the surface identifiability. The larger this nullity is, the less well constrained the inversion is, as a larger set of surfaces can produce the observations. Briefly, the dimension of a vector subspace is the number of linearly independent vectors needed to represent every vector in that subspace by linear combination. For example, in a two-dimensional Cartesian space, every point can be written as a combination of two basis vectors,  $x$  and  $y$ .

The null space can contain both individual spherical harmonics that produce no astrometric signal and specific linear combinations of spherical harmonics. If a single spherical harmonic for a certain  $(l, m)$  and inclinations  $\beta$  is in the null space:

$$A(\beta) \mathbf{e}_{l,m} = \mathbf{0},$$

Where  $\mathbf{e}_{l,m}$  denotes the basis vector with a single non-zero entry at  $(l, m)$ , corresponding to a surface made up solely of that single spherical harmonic mode. Other null space directions correspond to linear combinations of otherwise measurable harmonics whose contributions to the astrometric signal cancel exactly. To see how such degeneracies arise, consider the case  $\beta = 0$  (equator-on) described in Equation 11. All spherical harmonics  $Y_l^m$  of the same order  $m$  produce the same time-varying signal of the form  $e^{im\omega t}$ , weighted by different scalar kernel terms  $k_{l,m}^h$ . Thus, a surface consisting of a linear combination of order  $m$  harmonics can be constructed where the astrometric signal is zero even though the elements of  $\mathbf{s}$  are nonzero.

Instead of deriving the nullity by explicitly constructing a null space for each inclination, we obtain the nullity of  $A(\beta)$  directly from its rank via the rank-nullity theorem. The rank-nullity theorem states that for a linear matrix transform  $A(\beta) : \mathcal{C}^{(L+1)^2} \rightarrow \mathcal{C}^N$ ,

$$\text{nullity}(A(\beta)) + \text{rank}(A(\beta)) = (L+1)^2, \quad (16)$$

Here, we assume the number of measurements  $N > (L+1)^2$ . The  $\text{nullity}(A)$  is the number of linearly-independent vectors  $\mathbf{s} \in \mathcal{C}^{(L+1)^2}$  that are in the null-space of  $A(\beta)$ :  $A(\beta)\mathbf{s} = 0$ . Similarly, the  $\text{rank}(A(\beta))$  is the number of linearly independent columns or rows of  $A(\beta)$ . The dimension of the domain (i.e., the total number of spherical harmonic terms) is  $(L+1)^2$ .

The rank of  $A(\beta)$  for an order  $L$  spherical harmonic expansion is summarized in Table 2 for astrometry, photometry, and both measurements combined. Furthermore, in Figure 6, the nullity and rank of the forward model are shown for varying  $L$  and  $\beta$ . There are several key implications for surface mapping obtained from these results. First, the null space for photometry is larger than the null space for astrometry at all inclinations, meaning that photometric inversion carries less surface reconstruction power. Conversely, the rank of the photometry model is lower than that of the astrometry model. This is expected, since astrometry measurements have two degrees of freedom, whereas photometry measurements have only one. A higher rank means the null space is smaller and thus more information about the stellar surface can be gleaned. For both astrometry and photometry, the null-space is smallest at interior inclinations between 0 and  $\pi/2$  and largest at the pole. Second, since the dimension of  $\dim(\mathbf{s}) = (L+1)^2$  grows quadratically, while the model rank  $\propto L$  grows linearly for both photometry and astrometry, at a higher degree  $L$ , small spatial scale surface information is unrecoverable. This result was previously shown for photometry in [R. Luger et al. \(2021b\)](#). Below, we derive these results in detail.

Since  $A(\beta) = W_\omega B_\beta$ , the rank of  $A(\beta)$  is bounded as:

$$\text{rank}(A(\beta)) \leq \min(\text{rank}(W_\omega), \text{rank}(B_\beta)). \quad (17)$$

In the forward model, the surface coefficients are mapped onto a  $2 \cdot (2L+1) = 4L+2$  low-dimensional latent space via  $B_\beta$ , thereby bounding the model rank regardless of the total number of observations  $N$ . More measurements, however, will improve the signal-to-noise ratio. We assume  $N \geq 2L+1$  measurement times with uniform time-sampling to ensure  $W_\omega \in \mathcal{C}^{(2L+1) \times (2L+1)}$  is unitary and therefore rank-preserving when post-multiplying  $B_\beta$ , with  $\text{rank}(W_\omega) = (2L+1)$ , per  $x$  and  $y$  measurement. The matrix  $B_\beta \in \mathcal{C}^{(2L+1) \times (L+1)^2}$  and therefore  $\text{rank}(B_\beta) \leq (2L+1)$ . The rank of  $B_\beta$  depends on the inclination  $\beta$ . Note, the nullity must be derived jointly for  $x$  and  $y$  unless  $B_\beta^x$  and  $B_\beta^y$  are linearly independent, which is the case when  $\beta = 0$  but not guaranteed for other inclinations.

By inspection of Equations 11 and 12, for  $\beta = 0$  (equator-on), the null space includes all even degree- $l$  harmonics with  $l > 2$ , as well as specific linear combinations of harmonics that share the same azimuthal order  $m$  but differ in degree

$l$ . Among the azimuthal indices  $m \in [-L, L]$ , the number of odd values of  $m$  is  $2\lceil L/2 \rceil$  and the number of even values is  $2\lfloor L/2 \rfloor + 1$ . In addition,  $\mu^x$  is non-zero for two extra harmonics with  $(l, m) = (2, \pm 2)$ , while  $\mu^y$  measures two extra harmonics with  $(l, m) = (2, \pm 1)$ . Taken together, this yields  $\text{rank}(A(\beta = 0)) = 2L + 5$ . Applying the rank-nullity theorem in Equation 16, the null space therefore has dimension nullity  $(A(\beta = 0)) = (L + 1)^2 - (2L + 5) = L^2 - 4$ .

For inclinations  $\beta \in (0, \pi/2)$ , the inclination-dependent matrices,  $B_\beta^h$  for  $h \in \{x, y\}$ , have rank  $2L + 1$ . In Equation A7, these matrices are assembled from blocks  $C_\beta^l$  that mix the astrometric kernel terms  $\mathbf{k}_l^h$  across  $m \in \{-l, \dots, l\}$ . Each  $C_\beta^l$  is built from Wigner- $D$  matrices that are unique and of full rank. As a result, for inclined stars, all azimuthal orders  $m \in \{-l, \dots, l\}$  for odd degrees  $l$  contribute to the observed signal. The full forward matrix  $A(\beta) = W_\omega B_\beta$  has  $\text{rank}(A(\beta)) = 4L - 2$ . This is lower than the sum of the ranks of the  $x$  and  $y$  components because spherical harmonics of the degree  $l = L$ , order  $m = \pm L$  and  $m = \pm(L - 1)$  spherical harmonics produce identical  $x$  and  $y$  measurements up to a scaling, reducing the rank by 4. For  $\beta = \pi/2$  (pole-on) by inspection of Equation 13 and 14, both directions produce only a single  $m = \pm 1$  non-zero harmonic and  $\text{rank}(A(\beta = \pi/2)) = 2$ .

**Table 2.** Rank of the forward model  $\text{rank}(A(\beta))$  for astrometry, photometry, and astrometry/photometry measurements combined, for an order  $L > 2$  spherical harmonic expansion of the stellar surface. The size of the null space is  $(L + 1)^2 - \text{rank}(A(\beta))$ .

Inclination ( $\beta$ )	$\text{rank}(A_{\text{astro}}(\beta))$	$\text{rank}(A_{\text{photo}}(\beta))$	$\text{rank}(A_{\text{astro} \cap \text{photo}}(\beta))$
$\beta = 0$ (Face-on)	$2L + 5$	$L + 2$	$3L + 7$
$\beta \in (0, \pi/2)$ (Inclined)	$4L - 2$	$2L - 1$	$6L - 3$
$\beta = \pi/2$ (Pole-down)	2	1	3

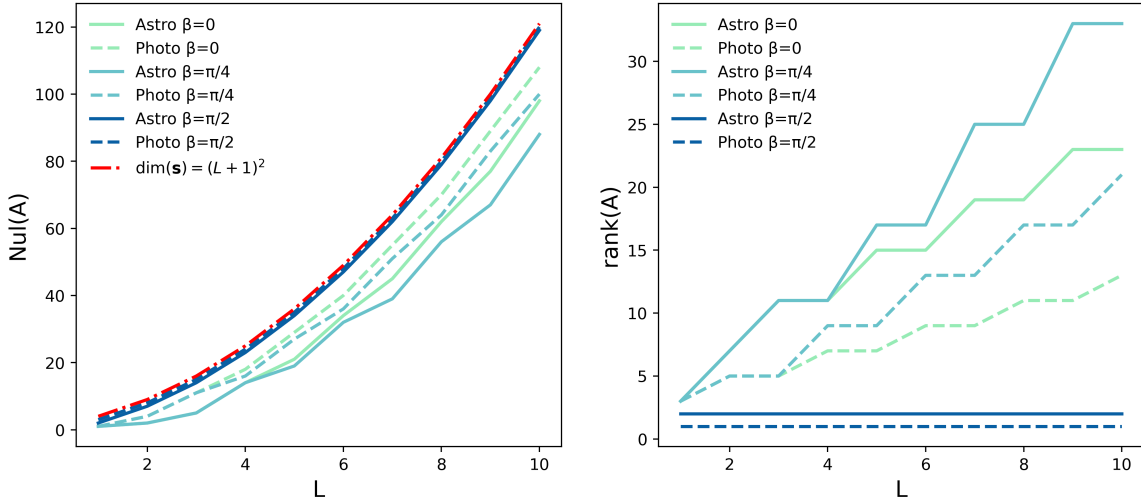


**Figure 6.** Comparing astrometry and photometry null space and rank across different inclinations. The size of the nullspace (left) is bounded by the total number of spherical harmonics (red line), and the rank (right), which quantifies the total information in the astrometric measurement. The astrometric operator has a higher rank than the photometric operator since it has two measurement directions; therefore, more information about the surface can be obtained. In general, both operators are highly rank-deficient relative to the total number of spherical harmonics  $(L + 1)^2$ , producing more degraded surface inversions.

### 2.3.2. Inclination identifiability

Above, we considered the surface inversion bias for a given inclination  $\beta$ . In this section, we consider estimating both the stellar surface  $\mathbf{s}$  and stellar inclination  $\beta$  jointly. Without additional constraints, the inclination cannot be uniquely identified, and consequently, neither can the stellar surface. In the forward model, an astrometric observation  $\mu$  is a linear combination of the columns of  $A(\beta)$  scaled by the surface spherical harmonic coefficient elements of  $\mathbf{s}$ .

The column space describes the set of all possible astrometric signals at a fixed inclination:

$$\text{col}(A(\beta)) = \{A(\beta)\mathbf{s} : \mathbf{s} \in \mathcal{C}^{(L+1)^2}\}. \quad (18)$$

If this set is invariant with inclination, then at any interior inclination  $\beta \in (0, \pi/2)$  there exists a surface  $\hat{\mathbf{s}}_\beta$  that can produce the same astrometric signal  $\mu$ :

$$\mu = A(\beta)\hat{\mathbf{s}}_\beta. \quad (19)$$

Thus, the inclination and the surface cannot be uniquely identified. To show the invariance of the column space, we apply the factorization of the forward model:

$$\text{col}(A(\beta)) = \text{col}(W_\omega B_\beta) = W_\omega \text{col}(B_\beta). \quad (20)$$

As described,  $B_\beta$  is rank deficient since 4 rows are linearly dependent between the sub-matrices  $B_\beta^x$  and  $B_\beta^y$ . The rows corresponding to spherical harmonic order  $m = \pm L$  and  $m = \pm(L-1)$  produce identical measurements up to a scaling, respectively in  $x$  and  $y$  measurement directions, reducing  $\text{rank}(B_\beta)$ . This is because only the  $l = L$  spherical harmonics contribute towards the non-zero elements of these rows. To show the invariance of  $\text{col}(B_\beta)$ , we consider a reduced version of the matrix  $B_\beta$  defined as  $\bar{B}_\beta = [B_\beta^x, B_\beta^y]^T$  where  $\bar{B}_\beta^x$  is absent the redundant first and last two rows of  $B_\beta^x$ . This new matrix  $\bar{B}_\beta \in \mathcal{C}^{(4L-2) \times (L+1)^2}$  has full row rank of  $4L-2$ , thus the column space spans  $\mathcal{C}^{4L-2}$ . The reduced matrix  $\bar{B}_\beta$  has the same information content as the full matrix  $B_\beta$ . Because the column space of the reduced matrix is invariant with  $\beta$ , so too is the column space of the full  $B_\beta$  and therefore  $A(\beta)$ . Consequently, the stellar inclination and the stellar surface are jointly unidentifiable.

To jointly estimate the pair  $(\mathbf{s}, \beta)$ , it is necessary to introduce a prior constraint on the surface solutions  $\mathbf{s}$  that breaks the degeneracy among surface solutions. This ensures the marginal Fisher information on inclination  $\beta$  is non-zero and the uncertainty of  $\beta$ , given by the reciprocal of the Fisher information, is bounded (J. Taaki et al. 2025). We do not additionally place a prior on the inclination; however, if partial information were known (such as from a  $v \sin i$  measurement (K. Masuda & J. N. Winn 2020)), this could be introduced as an additional constraint. The use of a prior might seem to imply an artificial bias of the surface solutions, but the properties of the prior needed to break the degeneracy can be very weak in practice. For example, a constraint that prevents a single spherical harmonic mode from dominating the solution will effectively steer the solution away from unphysical surfaces. The optimal choice of prior, which brings us closest to the true stellar inclination, will depend on the physical properties of the surface. In Section 3.2, we discuss the choice of surface prior applied herein.

### 3. ASTROPHYSICAL IMPLICATIONS

Above, we described the forward model for astrometric jitter measurements of a rotating star. Section 3.1 explores the implications of astrometric jitter by comparing the expected astrometric jitter amplitudes for main-sequence stars to the reflex motion amplitudes of habitable-zone exoplanets. In Section 3.2 we describe our approach to invert astrometric measurements and map the stellar surface. In Section 3.3, we demonstrate stellar surface mapping for astrometry and photometry, individually and combined.

#### 3.1. Starspot jitter and exoplanet astrometry

In this section, we introduce a simple framework for characterizing the amplitude of astrometric jitter as a function of starspot size, alongside planet-induced reflex motion. These can be compared to determine whether astrometric jitter will bias estimates of exoplanet mass. Furthermore, we use this to bound regions of the parameter space where starspots can be mapped with Gaia DR4 and DR5 precision. From M. Shao et al. (2009),  $\alpha$  is the amplitude of the astrometric reflex motion in microarcseconds of a star with mass  $M_\star$  at a distance  $D$  with a planet  $M_p$  orbiting with semi-major axis  $a$ :

$$\alpha = 3 \frac{M_\odot}{M_\star} \frac{M_p}{M_\oplus} \frac{a}{1 \text{ AU}} \frac{1 \text{ pc}}{D} \mu\text{as}. \quad (21)$$

For each main-sequence  $R_\star$ , we place the representative habitable-zone (HZ) semi-major axis at  $a_{\text{HZ}} \propto \sqrt{L_\star/L_\odot} \propto (M_\star/M_\odot)^{1.75}$ . Evaluating the astrometric amplitude expression in Equation 21 with  $a_{\text{HZ}}$  and using the mass-radius

relation, for an Earth-mass planet  $M_p = M_{\oplus}$ :

$$\alpha_{HZ} = 3 \frac{1 \text{ pc}}{D} \left( \frac{R_{\star}}{R_{\odot}} \right)^{0.94} \mu\text{as}. \quad (22)$$

To detect an Earth-mass planet orbiting in the HZ of a solar-mass star at 10 pc would require astrometric precision of  $\alpha_{HZ} = 0.3 \mu\text{as}$ . Next, we consider astrometric jitter as a source of error in weighing an Earth analog. We use the model for astrometric jitter due to a single starspot introduced by B. M. Morris et al. (2018). Similarly, we assume a single starspot at an equatorial latitude, the fractional flux change due to a starspot of radius  $R_{\text{spot}}$  is approximately  $F_{\text{spot}}/F_{\star} = CR_{\text{spot}}^2/R_{\star}^2$  where  $C$  is the wavelength-dependent spot-contrast. Starspot contrast is largest at bluer wavelengths (B. V. Rackham et al. 2023). We assume a Gaia  $G$ -band (330–1050 nm) and adopt a  $G$ -band spot contrast of  $C = 0.7$  based on B. M. Morris et al. (2018). Photo-center shift additionally scales with the angular radius of the star  $R_{\star}/D$ , the maximum astrometric jitter due to a starspot is  $\alpha_{\text{spot}} \approx \frac{F_{\text{spot}}}{F_{\star}} \frac{R_{\star}}{D} 4650 \mu\text{as}$ . This jitter model becomes inaccurate for spots that are large compared to the radius of the star. We consider starspots with  $R_{\text{spot}}$  up to  $0.3R_{\star}$  for which the astrometric approximation error is  $< 6\%$  (B. M. Morris et al. 2018).

Astrometric jitter can be a source of error in finding and measuring the masses of Earth like planets. Figure 7 illustrates the potential range in starspot-induced astrometric jitter noise as a heatmap where we span F,G,K,M stellar radii ( $0.5 - 1.7 R_{\odot}$ ) over the x-axis and starspot radius on the y-axis to ascertain starspot sizes that will produce significant sources of error. Exoplanet reflex motion amplitudes  $\alpha_{HZ}$  given by Equation 22 are overlaid on the heatmap as lines to illustrate where astrometric jitter will match the exoplanet signal. A starspot larger than 3% stellar radius will produce astrometric jitter of greater amplitude than an Earth-mass exoplanet orbiting in the habitable zone. This threshold does not change with stellar distance  $D$ , as both the astrometric jitter and the reflex motion amplitude are inversely proportional to  $D$ . A single starspot of size  $3\%R_{\star}$  will cover 0.1% of the visible hemisphere. Although measurements of smaller starspots of this scale are limited by observational sensitivity, larger regions of coverage have been commonly observed for magnetically active stars (K. G. Strassmeier 2009).

However, this is unlikely to be a significant source of uncertainty for the planet populations observable with Gaia since astrometric jitter will be below the Gaia measurement precision for the majority of targets. The end of mission (DR5) precision for targets with a magnitude of  $G = 13$  will be  $7 \mu\text{as}$ . (B. M. Morris et al. 2018) show that only nearby ( $< 10$  pc) active M/K dwarfs may have detectable star-spot induced astrometric jitter in forthcoming Gaia data release (DR4), where Gaia's precision reaches 3-5  $\mu\text{as}$ , shown in Figure 7. As given by Equation 21, reflex motion amplitude increases with planet mass and orbital separation. Considering low-mass planets that produce weak reflex motion signals, a Neptune-mass planet orbiting at 4 AU around a solar-mass star will need to be within  $D = 3.5$  pc to have a greater than 50% likelihood of detection in DR5 with  $\alpha \sim 50 \mu\text{as}$  (P. Ranalli et al. 2018). Thus, detecting low-mass planets in Gaia is likely to be rare. As described in T. D. Brandt (2024), Gaia is most sensitive to long orbital period (years) companions, peaking at planets with a 5.5-year and 10-year orbital period in DR4 and DR5, respectively. Recently C. Lammers & J. N. Winn (2025) reassessed the expected yield of Gaia, with 120,000 planet discoveries expected in DR5, with the majority having super-Jupiter-like masses.

Nevertheless, active nearby M dwarfs are a promising population for applying the astrometric mapping technique to probe magnetic activity. In total, there are 391 M dwarfs within 10 pc that will be observed by Gaia (C. Reylé et al. 2021). In addition, models of Solar-like stars predict that active G dwarfs with rotation periods of a few days can exhibit signatures of around  $15 \mu\text{as}$  at 10 pc, detectable with Gaia (K. Sowmya et al. 2022). Red supergiants (not shown over the range in Figure 7) may additionally show astrometric variability in Gaia data arising from large-scale convective surface structures ( Chiavassa, A. et al. 2022). Convection cells as large as 30 mas across have been detected on Betelgeuse via interferometry (A. Chiavassa et al. 2010).

### 3.2. Surface inversion

Starting with the signal model in Equation 8, we describe the procedure for generating a surface brightness map of the star from astrometric and photometric data. We first obtain a joint-likelihood function for the data, starting with the signal model and incorporating measurement noise, as well as a prior on the surface components to break the inclination degeneracy described in Section 2.3. Assuming additive, independent Gaussian noise with per-epoch variance  $\sigma^2$ ,  $\mathbf{n} \sim \mathcal{N}(\mathbf{0}, \sigma^2 I)$ , the astrometric measurements are given by:

$$\mathbf{y} = A(\beta)\mathbf{s} + \mathbf{n}. \quad (23)$$

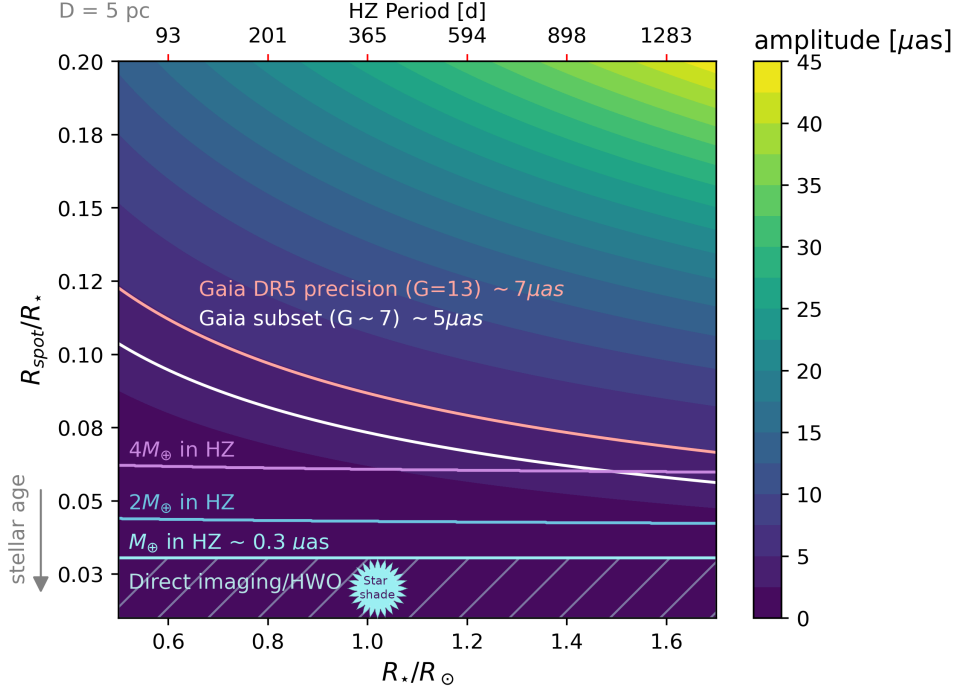


**Figure 7.** Astrometric jitter induced by starspots is a major source of error in precisely measuring mass. The jitter amplitude for a single starspot is shown as a heatmap as a function of starspot radius (y-axis) and stellar radius (x-axis), for a star at a distance of  $D = 5$  pc. The Gaia DR5 precision over the G-band for a  $G = 13$  magnitude star is also overlaid (dark orange), showing that if large starspots occur on these stars, they can be detected. Younger, magnetically active stars may have higher levels of starspot coverage. The astrometric precision for a subset of bright, nearby Gaia stars that are candidates for mapping, from B. M. Morris et al. (2018), is overlaid (white). For these stars, with starspots whose radii lie above this line, these are large enough to be mapped with Gaia data. Astrometric jitter is a limiting factor in measuring the masses of Earth analogs orbiting in the habitable zone (HZ). While Gaia is not sensitive enough to measure small HZ planets, future instruments aim to accomplish this. We illustrate this limiting error; overlaid are HZ exoplanet signal amplitudes for sub-Neptune-sized planets. The top x-axis shows the orbital period of a planet in the HZ as it scales with stellar radius. For starspots where the spot radius is above the exoplanet amplitude lines, astrometric jitter is larger in magnitude than the planet signal. At the Earth-mass level, relatively low levels of starspot coverage, unless corrected, may thus prohibit the identification of true Earth analogs in future surveys.

We assume the rotation period  $P$  of the star, or equivalently the rotation rate  $\omega = \frac{2\pi}{P}$ , is known or can reasonably be estimated via spectral techniques applied to light-curve or astrometry data (S. Aigrain et al. 2015; A. McQuillan et al. 2014). We use a Gaussian-Markov random field (GMRF) prior on the surface coefficients of the form  $\mathbf{s} \sim \mathcal{CN}(0, \Sigma)$ , where  $\Sigma$  is a diagonal covariance matrix that parameterizes a Gaussian-Markov random field. Several features of this prior make it suitable for describing a stellar surface. First, the prior is isotropic and does not bias the inversion towards a particular surface orientation. For a prior to be isotropic, it should be invariant at any location on the sphere. A Gaussian prior is completely parameterized by its mean and covariance. Thus, we can show it is isotropic by inspecting the rotation invariance of these parameters. The mean  $\mu_s$  (here taken to be 0) should be independent of spatial position and therefore constant. The covariance  $\Sigma$  in spherical harmonic coordinates must be invariant under any rotation. Since rotations are separable over degree  $l$ , we obtain a rotation of degree  $l$  coefficients  $\mathbf{s}_l$  through the Wigner D rotation matrix:  $D^l(R)\mathbf{s}_l$ . This is a linear transform of a Gaussian random vector, and therefore, the distribution of the rotated random vector is also Gaussian. Considering the covariance restricted to the degree  $l$  terms, the covariance of the rotated surface is  $D^l(R)\Sigma_l D^{l,T}(R)$ , and for this to be invariant under rotation, it must equal  $\Sigma_l$ . Only a scaled identity matrix of the form  $\Sigma_l = c_l I$  for some constant  $c_l$  will satisfy this rotation invariance. Equivalently, the spherical harmonic coefficients must be uncorrelated (J.-F. Cardoso 2010).

We next motivate the specific choice of degree-dependent scaling  $c_l$ . The GMRF prior corresponds to a quadratic penalty on the gradient of the surface in spatial coordinates, encouraging locally correlated structure while suppressing small-scale fluctuations. Under the GMRF prior, degree-dependent weights penalize higher degree coefficients. This is

appropriate, since the astrometric kernel weights decay with higher degree terms that correspond to finer spatial scales, and these components have lower SNR. Thus, downweighting these reduces the solution’s sensitivity to measurement noise. In particular, the GMRF parameterization used here per degree is  $\Sigma_l \propto (1/\lambda)(\gamma/l)^\alpha$ ,  $\gamma$  is an angular scale parameter, for  $\alpha > 1$ . Varying  $\alpha$  and  $\gamma$  controls the degree of angular scale correlation in spatial coordinates. Here,  $\lambda > 0$  is a regularization weight that controls the relative strength of the prior versus the data likelihood term. A similar scale-dependent prior is used in [B. Farr et al. \(2018\)](#) in the context of mapping exoplanets in reflected light, to enforce spatial correlations over spherical harmonic coordinates.

To obtain an estimate for the unknown surface and inclination, we maximize the likelihood of Equation 23, which is equivalent to minimizing the negative log-likelihood given by:

$$-\log p(\mathbf{y}, \mathbf{s} | \beta) \propto \underbrace{\frac{1}{\sigma^2} \|\mathbf{y} - A(\beta)\mathbf{s}\|_2^2}_{\text{data penalty}} + \underbrace{\mathbf{s}^H \Sigma^{-1} \mathbf{s}}_{\text{GMRF penalty}}. \quad (24)$$

This likelihood function consists of a data penalty term that depends on the data  $\mathbf{y}$ , and a GMRF penalty term on  $\mathbf{s}$ . To jointly minimize the negative log-likelihood over the surface coefficients  $\mathbf{s}$  and inclination  $\beta$ , we select the minimizing  $\hat{\mathbf{s}}_\beta$  computed for a discrete range of  $\beta \in [0, \pi/2]$ . For a fixed inclination  $\beta$ , the negative log-likelihood is minimized over  $\mathbf{s}$  by the regularized pseudoinverse of  $A(\beta)$  applied to the data  $\mathbf{y}$ :

$$\hat{\mathbf{s}}_\beta = (A(\beta)^H A(\beta) + \Sigma^{-1})^{-1} A(\beta)^H \mathbf{y}.$$

These surface estimates  $\hat{\mathbf{s}}_\beta$  will not have any component in the null space. This is because the GMRF penalty term in Equation 24 is non-negative for any  $\mathbf{s}$  and will increase for a null-space component, while having no effect on the data penalty. Therefore, a solution with a component in the null space will not be a minimizer of the negative log likelihood. We note the mean-square error between the estimated and true coefficients,  $\text{MSE} = \|\hat{\mathbf{s}} - \mathbf{s}\|_2^2 = \|\sum_{l,m} Y_l^m (\hat{s}_l^m - s_l^m)\|_2^2$  is equivalent to the surface estimation error, since the spherical harmonic transform is orthogonal and therefore preserves norms on vectors.

Using our likelihood model, it is possible to vary other parameters besides those pursued here. For example, the sky plane angle  $\alpha$  or the rotation rate  $\omega$ . Gradient-based optimization may be more appropriate for fitting multiple parameter values, particularly if their effect on the forward model is non-linear. Here,  $A(\beta)$  has a non-linear dependence on  $\beta$ . Still, because we only have one non-linear variable to solve for, it is simple to evaluate  $A(\beta)$  at different  $\beta$  values. In Appendix A.1, we provide the analytic derivative of  $A(\beta)$  with respect to  $\beta$ , which can be used to solve for  $\beta$  under a gradient-based optimization scheme. In [J. Taaki et al. \(2025\)](#), analytic Cramer-Rao bounds on the joint uncertainties of  $\mathbf{s}$  and  $\beta$  are derived. These show that under the joint-likelihood model, knowledge of the true inclination  $\beta$  improves the precision.

### 3.3. Reconstruction examples

In this section, we perform example surface inversions with simulated astrometric data. We simulate surfaces with a single starspot, generated with Starry ([R. Luger et al. 2019](#)), with the mean flux set to zero by the  $l = m = 0$  spherical coefficient. In Figure 8, the spherical harmonic coefficients for starspots of varying radii are visualized. Larger starspots have compact spherical harmonic representations, whereas smaller starspots have many non-zero coefficients. This behaviour is also observed in Fourier transforms ([D. L. Donoho & P. B. Stark 1989](#)). We simulate the astrometric and photometric signals for two surfaces with different starpot latitudes, sizes, and stellar inclinations. The first has an  $8\%R_\star$  sized starspot at a latitude of  $35^\circ$ , the second surface has a larger  $30\%R_\star$  starspot akin to that found on TOI-3884, at a latitude of  $50^\circ$ . To each of these surfaces, we add a randomly simulated GMRF surface. TOI-3884 is an M-dwarf at 43 pc with a large near-polar starspot that was detected through repeated transit crossings of TOI-3884b in TESS light curves ([J. M. Almenara et al. 2022; P. Tamburo et al. 2025](#)). Transit crossings of starspots can help constrain their latitudinal positions ([S. Sagynbayeva et al. 2025](#)). The transiting planet TOI-3884b has a 4.5 day orbital period with an estimated mass of  $32 M_\oplus$  from RV measurements ([J. E. Libby-Roberts et al. 2023](#)). The astrometric signature of TOI-3884b is of the order  $\alpha \sim 0.3\mu\text{as}$  as the star is at a distance of 43.34 pc. At this near polar latitude, the peak-to-peak jitter due to the sparspot is approximately  $\sim 0.3\mu\text{as}$ . While this system is below Gaia’s sensitivity, it serves as an example of a known system in which star-spot-induced astrometric jitter would be a potential source of error in measuring planet mass.

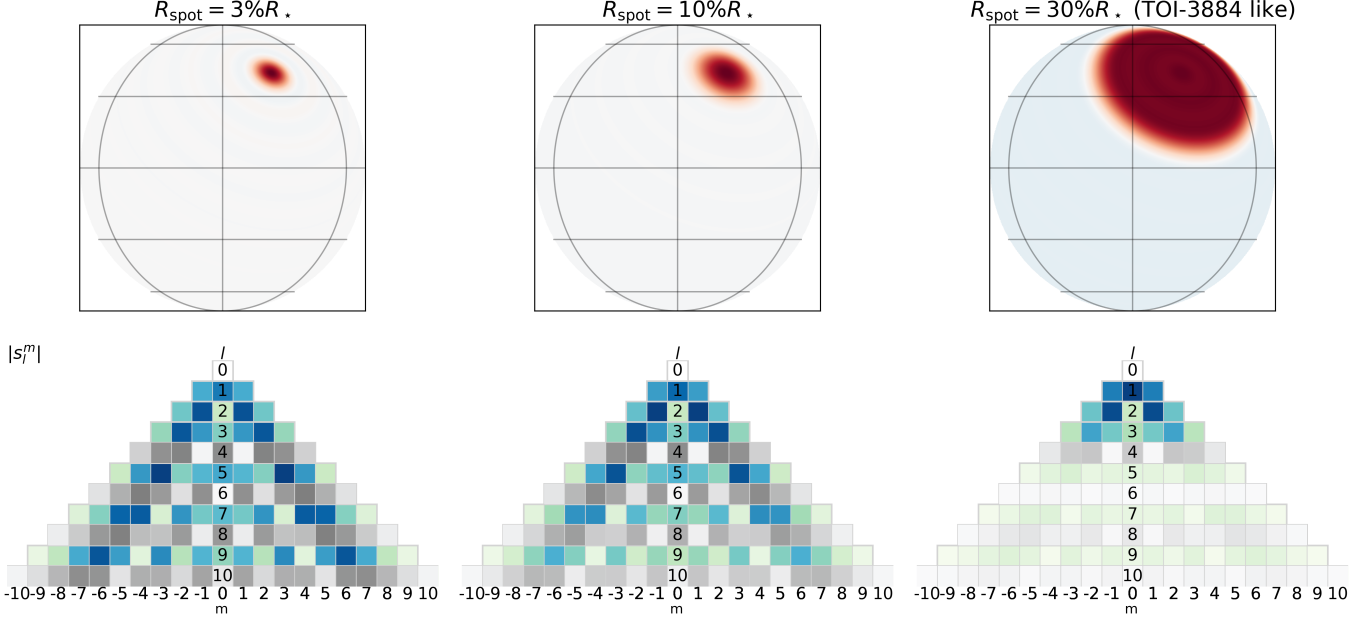


**Figure 8.** Visualizing the starspot coefficients for starspots of varying radii. The surface is shown equator-on up to degree  $L = 25$  (top row) and the corresponding surface coefficients  $\mathbf{s}$  up to degree  $L = 10$  (bottom row). The surface coefficients that do not contribute to the astrometric measurements and belong to the nullspace are shown in grey. Additionally, we have set the mean flux term to zero ( $s_0^0 = 0$ ), as it is much larger in magnitude than the other signal components. These illustrate the Fourier uncertainty principle: smaller, more compact starspots have larger spherical harmonic representations.

When performing the surface inversion, the maximum spherical harmonic degree  $L$  must be specified. The number of observations  $N$  both limits the signal-to-noise ratio, as well as the maximum degree  $L$  that can be resolved without aliasing. According to the Shannon-Nyquist sampling theorem (A. Oppenheim 1993), to resolve a signal without aliasing, the sampling frequency  $f_s$  must satisfy  $f_s > 2f$ , where  $f$  is the highest frequency component of the signal. The astrometric time-series signals in  $x$  and  $y$  (Equation 8) are sinusoids composed of conjugate sums of complex exponential oscillations. The highest temporal frequency present occurs for a spherical harmonic of order  $m = L$ , to resolve this, we then require  $N > 2L$ . Equivalently, if we have some  $N = 31$  measurements, we may only resolve up to  $L = 15$  spherical harmonics. If  $L > \frac{N}{2}$ , the contribution of higher-order harmonics will appear as if a lower-order term created it, so smaller-scale surface features will project to larger-scale terms. In this example, we simulate  $N = 100$  and choose  $L = 10$  for both the simulation and inversion, below the aliasing cutoff. Without loss of generality, we take the orbital period as  $P = 1$ .

For each simulated surface, we apply the Bayesian approach described in 3.2 to estimate the stellar surface and inclination, using the same GMRF prior and hyperparameter values for both photometry and astrometry data. We use the following parameter values:  $\lambda = 10^{-4}$ ,  $\gamma = 2$ ,  $\alpha = 1$ . The GMRF prior used here is invariant with spatial position and can encompass a broad range of surface features. We use this inversion technique for astrometry alone, for photometry alone, and for combined astrometry and photometry data. The ground truth simulated stellar surfaces and reconstructions are shown in Figure 9. Identifying spot latitude and stellar inclination with photometry is known to be degenerate. In the reconstructions from photometry, the surface features are smeared latitudinally, reflecting this uncertainty. Astrometry reconstructions provide better constraints on stellar inclination and spot latitude than photometry reconstructions. When photometry and astrometry data are combined, inclination accuracy improves further, as does the overall surface reconstruction accuracy.

#### 4. CONCLUSION

To examine astrometric jitter induced by starspots on an inclined, rotating stellar surface, we derived an analytic forward model that is linear in the spherical-harmonic representation of the stellar surface (Section 2). The astrometric response to each static spherical harmonic is the astrometric kernel, which serves as the foundation of this model. A full astrometric time series is generated as a linear combination of the astrometric kernel terms. Although astrometric

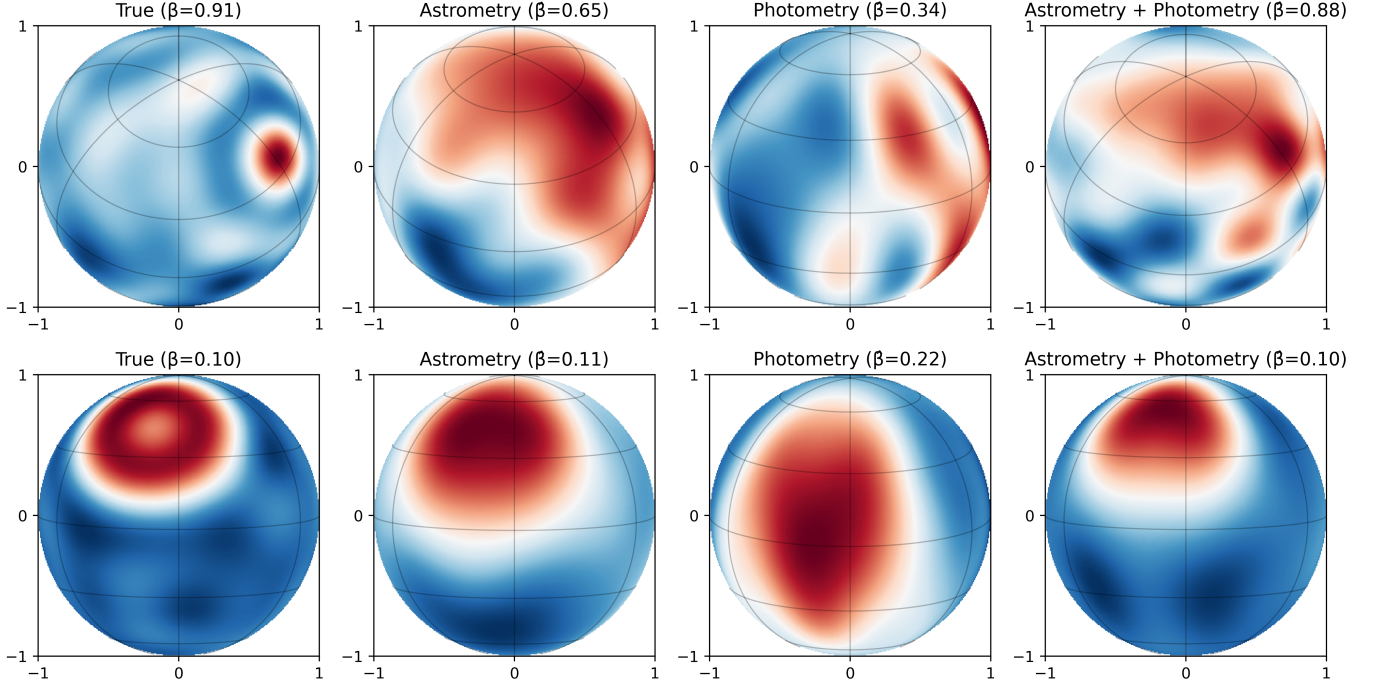


**Figure 9.** Two example reconstructions for a simulated 8%  $R_*$  starspot (top row) and a TOI-3884 like 30%  $R_*$  starspot (bottom row). The first column shows the ground truth simulated surface at the true inclination angle, represented by a truncated spherical harmonic expansion up to  $L = 10$ . Reconstructions of the surface and inclination  $\beta$  (assumed unknown) are shown using astrometry mapping (column two), photometry mapping (column three), and combined astrometry-photometry mapping (column four). All solutions use the same regularized least-squares inversion approach described in Section 3.2. Here, the photometric surface reconstructions tend to be smeared latitudinally, reflecting an inherent degeneracy in identifying spot latitude and stellar inclination with photometry. The astrometric reconstruction shows a localized starspot and better constraints on stellar inclination. Combining astrometry and photometry improves the accuracy of inclination and latitude by providing complementary information.

jitter is a source of noise in measuring exoplanet-induced reflex motion, we show that this forward model can be inverted, allowing jitter signals to be used to map stellar surfaces.

Light-curve inversion has been widely used for mapping stellar surfaces, but it suffers from degeneracies, particularly in constraining spot latitude (Z. Eker 1996; Z. Kovari & J. Bartus 1997; L. M. Walkowicz et al. 2013; J. R. A. Davenport et al. 2015; R. M. Roettenbacher et al. 2017). Using the astrometric kernel, we demonstrate that astrometry (first moments of a stellar point-spread function) measures a different set of spherical-harmonic surface modes than light curves (zeroth moments), thereby breaking degeneracies in surface mapping with photometry alone. Light curve data measures even-degree  $l$  harmonics that are symmetric about the equator (N. B. Cowan et al. 2013b). In contrast, astrometry measures odd-degree  $l$  harmonics that are antisymmetric about the equator and introduce asymmetries in the photo-center. Furthermore, astrometry measures two independent components of the photo-centre motion ( $x$  and  $y$ ), providing information that constrains both latitude and longitude of a starspot. In spherical-harmonic terms, for a star viewed from the equator, among odd-degree  $l$  harmonics, the  $x$  direction component measures odd-order  $m$  harmonics and the  $y$  direction, even-order  $m$  harmonics, while photometry only measures even degree  $l$  and even-order  $m$  harmonics. For a star with an inclined rotational axis, photometry and astrometry remain complementary by still only observing even- and odd-degree spherical harmonics, respectively. This means that when astrometry and photometry measurements are combined, both contribute unique information about the stellar surface, thus improving the surface inversion accuracy. However, the sensitivity of photometry and astrometry to spherical harmonic order  $m$  changes with inclination. Through quantifying the resulting change in the rank of the forward model, we show that interior inclinations  $\beta \in (0, \pi/2)$  carry the most recoverable surface information. A larger rank equates to a smaller nullspace, meaning fewer possible stellar surfaces can produce the measured astrometric signal, and the surface inversion is better constrained. Interior inclinations achieve a substantially higher rank ( $\sim 4L$ ) than equator-on ( $2L$ ) or pole-on limits (2), which carry less information for both astrometry and photometry. Viewing the star pole-on

carries the least surface information, and any astrometric signal will be purely circular, while photometry can only obtain the mean flux.

In Section 3.2, we introduce a Bayesian inversion approach to estimate both stellar inclination and the surface brightness map of the star, since without any constraints, the stellar inclination is shown to be unidentifiable. Equivalently, for every possible inclination  $\hat{\beta}$ , there is a stellar surface  $\mathbf{s}_{\hat{\beta}}$  that can exactly reproduce the astrometric signal  $\boldsymbol{\mu}$  from the true inclination  $\beta$ . To render the inclination identifiable, we introduce a spatial-scale-dependent prior on the stellar surface (J. Taaki et al. 2025). This Gaussian-Markov-Random-Field (GMRF) prior encourages locally correlated, piecewise-smooth structure while still permitting sharp discontinuities in the surface amplitude, for example, at the edge of a spot. By imposing a GMRF prior, the posterior Fisher matrix is non-zero and yields finite precision bounds for both the surface and the inclination.

However, even under a constrained starspot model, fitting the starspot to light-curve data is degenerate with respect to spot latitude and stellar inclination (Z. Eker 1996; Z. Kovari & J. Bartus 1997; L. M. Walkowicz et al. 2013). We perform example surface inversions with both light curves and astrometry data under the Bayesian GMRF prior. Our simulations show that astrometry retrieves two directions of information and can reliably localize the spot position alongside stellar inclination, whereas photometric reconstructions tend to be smeared latitudinally. When astrometry and photometry are combined, overall reconstruction accuracy improves. Constraints on stellar inclination through astrometric jitter may provide a new angle for studying spin-orbit misaligned systems (S. H. Albrecht et al. 2022).

As shown in Figure 7, a single starspot with a radius  $3\%R_{\star}$  or larger may create jitter at the amplitude as the reflex motion due to an Earth-mass exoplanet orbiting in the habitable zone. While interior inclinations are optimal for surface mapping, K. Sowmya et al. (2021) find that these non-equatorial astrometric jitter signals are harder to disambiguate from planet-induced reflex motion. Non-equatorial inclinations, however, are optimal for direct imaging of exoplanets in reflected light. Future direct-imaging missions, such as the Habitable Worlds Observatory, can take days to weeks to image an exoplanet in reflected light (B. Mennesson et al. 2024). As K. E. Painter et al. (2025) describes, they are most efficient when they can target systems with precursor astrometric detections of planets and constrained planetary masses. Our model quantifies the variations in astrometric jitter with inclination angle, providing an analytical foundation for studying starspot noise in astrometry, worst-case geometries, and their impact on exoplanet mass measurements in future sub- $\mu$ as astrometry. In future work, we aim to use the inversion framework to jointly fit reflex motion and stellar surfaces and to quantify the impact on mass-estimator precision.

In Figure 7, the expected level of astrometric jitter for bright stars at a distance of 5 pc in Gaia data is visualized. A single large starspot with a radius that lies above the curve ( $> 10\%R_{\star}$  for an M-dwarf) can exhibit detectable jitter. There are 391 M-dwarfs within 10 pc (C. Reyé et al. 2021) to which the astrometric mapping techniques described herein can be applied with upcoming Gaia data releases. Because starspots also bias radial-velocity and transmission-spectroscopy measurements (B. V. Rackham et al. 2023), improved stellar surface mapping can help correct biases across various measurements for the mapped stars. In particular, the Transit Light Source Effect (TLSE) biases transit-depth measurements by altering the measured stellar spectrum across the occulted and unocculted regions (B. V. Rackham et al. 2018).

A limitation of this work is that we have not incorporated limb darkening or extended our analysis to multiple observing bands. These factors may change the identifiability of surfaces. R. Luger et al. (2021b) consider quadratic limb darkening in the context of photometry and find a non-trivial impact on the forward model, which varies with the assumed limb-darkening model. In future work, we will incorporate quadratic limb darkening into the astrometric operator and obtain an astrometric kernel under this setting. Besides limb darkening, stars exhibit differential rotation and have non-static surfaces. J. R. A. Davenport et al. (2015) use four years of Kepler observations to detect differential rotation and starspot evolution. By breaking latitude degeneracies, astrometric surface mapping may offer a valuable probe of differential rotation, but extending our framework to time-variable surfaces will be necessary to interpret longer-baseline observations, as expected with upcoming Gaia data.

<sup>1</sup> This project is supported by the Eric and Wendy Schmidt AI in Science Postdoctoral Fellowship, a program of Schmidt Sciences. This research was partially supported by grant CCF-2246213 from the National Science Foundation.

*Software:* Sympy (A. Meurer et al. 2017), Starry (R. Luger et al. 2019)

This appendix derives the forward model summarized in Section 2 and provides the technical details. We first describe the rotation formalism used to express astrometric first moments in spherical-harmonic space, including the decomposition that isolates the inclination angle (Appendix A). We then derive the gradient of the forward model with respect to inclination (Appendix A.1), followed by the construction of the astrometric kernel and its role in the forward model (Appendix B).

### A. INCLINED ROTATION

We define  $h \in \{x, y\}$  as the projected x and y-coordinates from the observer's perspective. A first-order moment measurement  $\mu^h : h \in \{x, y\}$  at a rotation  $R = (\alpha, \beta, \gamma)$  for stellar surface spherical harmonic coefficients  $\mathbf{s}$  is given by:

$$\mu^h(R) = \sum_{l \geq 0} \langle \mathbf{s}_l, D^{l,H}(R) \mathbf{k}_l^h \rangle \quad (\text{A1})$$

The Wigner D rotation matrix is:

$$D_{mm'}^l(\alpha, \beta, \gamma) = e^{-im\alpha} d_{m,m'}^l(\beta) e^{-im'\gamma}. \quad (\text{A2})$$

which introduces inclination  $\beta$  through the small Wigner D terms:  $d_{m,m'}^l(\beta)$ . We take  $\alpha = 0$  and  $\beta$  is the unknown inclination angle. We take  $\gamma = \omega t$  and assume  $\omega$  is known.

In our forward model, we utilize the conjugate transpose of the rotation:  $D^{l,H}(\alpha, \beta, \gamma) = D^l(-\gamma, -\beta, -\alpha)$ . Evaluated as is, the inclination depends on small Wigner D terms  $d_{m,m'}^l(-\beta)$ . We modify the identity from [A. Makadia & K. Daniilidis \(2003\)](#) to rewrite the first rotation  $D^l(0, -\beta, 0)$  in a form that is simple to differentiate with respect to inclination:  $D^l(0, -\beta, 0) = D_2^l(\pi/2 - \pi/2, \pi/2, 0) D_1^l(\beta + \pi, \pi/2, \pi/2)$ . By decomposing the inclination rotation into two components,  $D_1$  and  $D_2$ , we effectively isolate the parameter  $\beta$  within  $D_2$ , allowing for a straightforward computation of the partial derivative with respect to  $\beta$ , while avoiding the direct use of small Wigner D-matrix terms  $d_{m,m'}^l(\beta)$  whose derivatives rely on complex recurrence relations.

Considering a single  $l$ , we can write the Wigner-D rotation of the kernel  $\mathbf{k}_l$  as:

$$[D^l(R) \mathbf{k}_l]_m = \sum_{m'=-l}^l D_{m,m'}^l(\alpha, \beta, \gamma) k_{l,m'} \quad (\text{A3})$$

$$= e^{-im\alpha} \sum_{m'=-l}^l d_{m,m'}^l(\beta) e^{-im'\gamma} k_{l,m'} \quad (\text{A4})$$

$$= e^{-im\alpha} \sum_{m'=-l}^l C_{\beta, m, m'}^l k_{l,m'} \quad (\text{A5})$$

Define  $C_{\beta}^l = D_1^l D_2^l(\beta) \in \mathcal{C}^{(2l+1) \times (2l+1)}$ . Inclination mixes orders  $m \in \{-l \dots l\}$  within each  $l$  as  $\mathbf{k}_l^h = C_{\beta}^l \mathbf{k}_l^h$ . For simplicity, take  $\gamma = 0$  (the rotation in the sky plane). Equation A1 describes the measurement at a single rotation, the time-dependent rotation factor  $\exp^{-im\alpha}$  can be pulled outside summation over  $l$ .

$$\mu^h(R) = \sum_m e^{-im\alpha} \left[ \sum_l C_{\beta}^l \mathbf{k}_l^h \odot \mathbf{s}_l \right]_m \quad (\text{A6})$$

The  $\odot$  symbol here denotes the Hadamard product, the element-wise product of two vectors. For  $N$  astrometric observations over time  $\boldsymbol{\mu}^h = [\mu^h(t_1), \dots, \mu^h(t_N)]^T$ :

$$\boldsymbol{\mu}^h = W_{\omega} \sum_l C_{\beta}^l \mathbf{k}_l^h \odot \mathbf{s}_l, \quad (\text{A7})$$

$$\boldsymbol{\mu}^h = W_{\omega} B_{\beta}^h \mathbf{s}. \quad (\text{A8})$$

The reduced form in Equation A8 is obtained by using an identity for a Hadamard product and separates the forward model into a time-dependent component  $W_{\omega} \in \mathcal{C}^{N \times 2l+1}$  and an inclination, as well as observational direction  $h \in \{x, y\}$ ,

dependent matrix  $B_\beta^h \in \mathcal{C}^{(2l+1) \times (l+1)^2}$ . The matrix  $B_\beta^h$  captures the astrometric kernel  $\mathbf{k}_l^h$  information, as a row-block matrix of diagonalized vectors over  $l$ :

$$B_\beta^h = [\text{diag}(C_\beta^0 \mathbf{k}_0^h), \dots, \text{diag}(C_\beta^L \mathbf{k}_L^h)]. \quad (\text{A9})$$

For a different measurement kernel, i.e., the zeroth moment (photometry), the corresponding kernel can be dropped in to this measurement model without any changes. The matrix  $W_\omega \in \mathcal{C}^{N \times (2l+1)}$  encapsulates the time dependence. We assume a full rotation is observed with uniform points although this can easily be modified to handle arbitrary points in time.  $W_\omega$  is a Vandermonde-like matrix whose columns are harmonics:

$$W_\omega = \begin{bmatrix} \lambda^{0 \cdot (-l)} & \lambda^{0 \cdot (-l+1)} & \dots & \lambda^{0 \cdot l} \\ \lambda^{1 \cdot (-l)} & \lambda^{1 \cdot (-l+1)} & \dots & \lambda^{1 \cdot l} \\ \vdots & \vdots & \ddots & \vdots \\ \lambda^{(N-1) \cdot (-l)} & \lambda^{(N-1) \cdot (-l+1)} & \dots & \lambda^{(N-1) \cdot l} \end{bmatrix},$$

where  $\lambda = e^{-i2\pi\omega/N}$ , when  $N \geq (L+1)^2$  this matrix is unitary and  $W_\omega^H W_\omega = N I_{(L+1)^2}$ .

### A.1. Inclination gradient

We state the analytic gradient of  $\boldsymbol{\mu} = A(\beta)\mathbf{s}$  with respect to inclination  $\beta$ . We use this to derive the Fisher information for  $\beta$  and  $\mathbf{s}$ .

With  $A(\beta) = W_\omega B_\beta$ :

$$\frac{\partial \boldsymbol{\mu}^h}{\partial \beta} = W_\omega \frac{dB_\beta^h}{d\beta} \mathbf{s}, \quad (\text{A10})$$

$$\frac{dB_\beta^h}{d\beta} = [\text{diag}(\frac{dC_\beta^0}{d\beta} \mathbf{k}_0^h) \dots \text{diag}(\frac{dC_\beta^L}{d\beta} \mathbf{k}_L^h)], \quad (\text{A11})$$

$$\frac{dC_\beta^l}{d\beta} = -i D^l(\frac{\pi}{2}, \frac{\pi}{2}, 0) \text{diag}(-l, \dots, l) D^l(\beta + \pi, \frac{\pi}{2}, \frac{\pi}{2}). \quad (\text{A12})$$

where  $D^l$  are Wigner D matrices.

## B. ASTROMETRY KERNEL

We derive the forward astrometry model using the Wigner-D rotations applied to an astrometric kernel, described above in Appendix A. To derive the astrometric kernel, our approach follows a similar derivation and conventions to those used for photometry measurements in N. B. Cowan et al. (2013b). The  $\mathbf{k}_l^x$  and  $\mathbf{k}_l^y$  vectors for the forward model are the first-moments  $k_{l,m}^h = \mathcal{A}_h(Y_l^m(\theta, \phi))$  of each spherical harmonic with no rotation, i.e., inclination  $\beta = 0$  corresponding to an equatorial observer and  $t = 0$ , where  $\mathbf{k}_l^h : h \in \{x, y\}$  denotes the vector of coefficients  $k_{l,m}^h$  for  $m = -l$  to  $l$ .

$$k_{l,m}^x = \int x_{obs}(\theta, \phi) V(\theta, \phi) Y_l^m(\theta, \phi) d\Omega, \quad (\text{B13})$$

$$k_{l,m}^y = \int y_{obs}(\theta, \phi) V(\theta, \phi) Y_l^m(\theta, \phi) d\Omega, \quad (\text{B14})$$

with  $d\Omega = \sin(\theta) d\theta d\phi$  and integration limits  $\theta \in [0, \pi]$ ,  $\phi \in [-\pi/2, \pi/2]$  reflecting the visible hemisphere. The astrometric weightings  $x_{obs}(\theta, \phi)$  and  $y_{obs}(\theta, \phi)$  are the projected x and y-coordinates from the observers perspective.  $V(\theta, \phi)$  is the visibility from the observers perspective, a point on the surface is visible if the inner product between its coordinates and the observer coordinates is positive:

$$\sin(\theta) \sin(\theta_0) \cos(\phi - \phi_0) + \cos(\theta) \cos(\theta_0) \geq 0, \quad (\text{B15})$$

The observer lies along the x-axis facing the equator at position  $\theta_0 = \pi/2, \phi_0 = 0$ .

$$V_{\beta=0} = \frac{1}{\pi} \sin(\theta) \cos(\phi) \quad (\text{B16})$$

for  $\theta \in [0, \pi], \phi \in [-\pi/2, \pi/2] : V_{\beta=0}(\theta, \phi) \geq 0$ , normalized to represent the visible hemisphere's solid angle. For an observer along the x-axis,  $x_{obs}$  and  $y_{obs}$  correspond to the 3D  $y, z$  coordinates. These are  $x_{obs} = \sin(\phi) \sin(\theta)$  and  $y_{obs} = \cos(\theta)$ . Hereinafter, we drop the indices on  $x_{obs}$  and  $y_{obs}$  and use  $x$  and  $y$  to refer to the observer's sky-plane coordinates.

### B.1. Deriving the kernel as static first order moments of the spherical harmonics

The first moment in  $x$  is:

$$k_{l,m}^x = \frac{1}{\pi} \int \sin(\theta) \sin(\phi) \sin(\theta) \cos(\phi) Y_l^m(\theta, \phi) d\Omega \quad (\text{B17})$$

$$k_{l,m}^x = \underbrace{\frac{N_l^m}{\pi} \int_0^\pi \sin^3 \theta P_l^m(\cos \theta) d\theta}_{I_{u,x}(l,m)} \cdot \underbrace{\int_{-\pi/2}^{\pi/2} \sin \phi \cos \phi e^{im\phi} d\phi}_{I_{\phi,x}(m)}. \quad (\text{B18})$$

The second integral over  $\phi$  can be expanded as:

$$I_{\phi,x}(m) = \int_{-\pi/2}^{\pi/2} \sin(\phi) \cos(\phi) (\cos(m\phi) + i \sin(m\phi)) d\phi \quad (\text{B19})$$

The first term in this integral is over an anti-symmetric function for all  $m$ , therefore it is always 0. The second integral is always 0 for  $m = 0$ , it additionally is 0 for even  $m > 2$ .

$$I_{\phi,x}(m) = i \int_{-\pi/2}^{\pi/2} \sin \phi \cos \phi \sin(m\phi) d\phi = \begin{cases} \frac{i\pi}{4}, & m = \pm 2, \\ -\frac{2i \sin\left(\frac{\pi m}{2}\right)}{m^2 - 4}, & m \neq \pm 2 \text{ and } m \text{ odd}, \\ 0, & m > 2 \text{ even.} \end{cases} \quad (\text{B20})$$

The first integral in Equation B18,  $I_{u,x}(l, m)$ , is re-parameterized with  $u = \cos(\theta)$  and  $du = \frac{-d\theta}{\sin(\theta)}$ :

$$I_{u,x}(l, m) = \int_0^\pi \sin^3(\theta) P_l^m(\cos(\theta)) d\theta \rightarrow \int_{-1}^1 (1 - u^2) P_l^m(u) du \quad (\text{B21})$$

Since  $1 - u^2$  is symmetric over the domain  $[-1, 1]$  and the Legendre polynomials  $P_l^m$  are antisymmetric when  $l - m$  is odd, this integral is 0 when  $l - m$  is odd and non-zero for  $l - m$  even. Combining these restrictions,  $k_{l,m}^x$  is 0 when  $l > 2$  is even (for all  $m$ ), or when  $m > 2$  is even, also for all  $l, m = \pm 1$  and  $l, m = \pm 2$ .

Similarly we derive the first moment in  $y$  as:

$$k_{l,m}^y = \frac{N_l^m}{\pi} \underbrace{\int_0^\pi \cos \theta \sin^2 \theta P_l^m(\cos \theta) d\theta}_{I_{u,y}(l,m)} \cdot \underbrace{\int_{-\pi/2}^{\pi/2} \cos \phi e^{im\phi} d\phi}_{I_{\phi,y}(m)}. \quad (\text{B22})$$

Taking a closer look at the second integral in  $\phi$ :

$$I_{\phi,y}(m) = \int_{-\pi/2}^{\pi/2} \cos(\phi) (\cos(m\phi) + i \sin(m\phi)) d\phi = \int_{-\pi/2}^{\pi/2} \cos(\phi) \cos(m\phi) d\phi \quad (\text{B23})$$

This integral evaluates to zero for odd  $m > 1$ .

$$I_{\phi,y}(m) = \int_{-\pi/2}^{\pi/2} \cos \phi \cos(m\phi) d\phi = \begin{cases} \frac{\pi}{2}, & m = \pm 1, \\ -\frac{2 \cos\left(\frac{\pi m}{2}\right)}{m^2 - 1}, & m \neq \pm 1 \text{ and } m \text{ even,} \\ 0, & m > 1 \text{ odd.} \end{cases} \quad (\text{B24})$$

The first integral  $I_{u,y}(l, m)$  is:

$$I_{u,y}(l, m) = \int_0^\pi \cos(\theta) \sin^2(\theta) P_l^m(\cos(\theta)) d\theta \rightarrow \int_{-1}^1 x \sqrt{1 - u^2} P_l^m(u) du \quad (B25)$$

The function  $u\sqrt{1 - u^2}$  is antisymmetric over  $[-1, 1]$ , and when  $l - m$  is even  $P_l^m$  is symmetric and the integral is zero. Therefore  $k_{l,m}^y$  are zero when  $l > 2$  are even or  $m$  are odd. The final kernel form is summarized in Equations 10. The values of  $\mathbf{k}_l^h : h \in \{x, y\}$  are integrated numerically with Sympy and shown in Figure 4 for  $l \leq 7$ .

### B.2. First-order moments viewed face-on

The time-dependent first-moment for inclination  $\beta = 0$ , of a spherical harmonic index by  $l, m$  is given by Equation A4 noting  $d_{m,m'}(\beta = 0) = \delta_{m-m'}$ , so that:

$$\mu_{l,m}^x(t) = e^{-im\omega t} k_{l,m}^x, \quad (B26)$$

$$\mu_{l,m}^y(t) = e^{-im\omega t} k_{l,m}^y. \quad (B27)$$

### B.3. First-order moments viewed from pole

The time-dependent moments are found by evaluating an inclination-dependent rotation of  $\mathbf{k}_l^h : h \in \{x, y\}$  and then using the  $m^{th}$  rotated component to weight a linear combination of harmonics of the form  $e^{im\omega t}$ . The inclination-dependent rotation is given by the summation in Equation A8,  $\sum_{m'=-l}^l d_{l,m'}^l(\beta = \pi/2) k_{l,m'}^h$ . At this inclination  $d_{m,m'}^l(\beta = \pi/2)$  is non-zero only when  $m = \pm 1$ . This summation is non-zero only for  $m = \pm 1$ .

$$p_{l,m=1}^h = \sum_{m'=-l}^l d_{l,m'}^l(\beta = \pi/2) k_{l,m'}^h, \quad (B28)$$

and  $p_{l,m=-1}^h = -p_{l,m=1}^h$  for  $h \in \{x, y\}$

$$\mu_{l,m}^x(t) = \begin{cases} p_{l,m}^x e^{i\omega t} & \text{if } l > 2 \text{ is odd, } m = \pm 1 \\ 0 & \text{otherwise,} \end{cases} \quad (B29)$$

$$\mu_{l,m}^y(t) = \begin{cases} p_{l,m}^y e^{i\omega t} & \text{if } l > 2 \text{ is odd, } m = \pm 1 \\ 0 & \text{otherwise,} \end{cases} \quad (B30)$$

## REFERENCES

Aigrain, S., Llama, J., Ceillier, T., et al. 2015, Testing the recovery of stellar rotation signals from Kepler light curves using a blind hare-and-hounds exercise, *Monthly Notices of the Royal Astronomical Society*, 450, 3211, doi: [10.1093/mnras/stv853](https://doi.org/10.1093/mnras/stv853)

Albrecht, S. H., Dawson, R. I., & Winn, J. N. 2022, Stellar Obliquities in Exoplanetary Systems, *Publications of the Astronomical Society of the Pacific*, 134, 082001, doi: [10.1088/1538-3873/ac6c09](https://doi.org/10.1088/1538-3873/ac6c09)

Almenara, J. M., Bonfils, X., Forveille, T., et al. 2022, TOI-3884 b: A rare 6- $R_E$  planet that transits a low-mass star with a giant and likely polar spot, *A&A*, 667, L11, doi: [10.1051/0004-6361/202244791](https://doi.org/10.1051/0004-6361/202244791)

Bao, C., Ji, J., Tan, D., et al. 2024, Closeby Habitable Exoplanet Survey (CHES). I. Astrometric Noise and Planetary Detection Efficiency Due to Stellar Spots and Faculae, *The Astronomical Journal*, 167, 286, doi: [10.3847/1538-3881/ad4031](https://doi.org/10.3847/1538-3881/ad4031)

Basri, G., & Shah, R. 2020, The Information Content in Analytic Spot Models of Broadband Precision Light Curves. II. Spot Distributions and Lifetimes and Global and Differential Rotation, *The Astrophysical Journal*, 901, 14, doi: [10.3847/1538-4357/abae5d](https://doi.org/10.3847/1538-4357/abae5d)

Bendek, E., Mamajek, E., Vasisht, G., et al. 2021, in American Astronomical Society Meeting Abstracts, Vol. 237, American Astronomical Society Meeting Abstracts #237, 318.02

Bendek, E. A., Guyon, O., Ammons, S. M., & Belikov, R. 2013, Laboratory Demonstration of Astrometric Compensation Using a Diffractive Pupil, *Publications of the Astronomical Society of the Pacific*, 125, 1212, doi: [10.1086/673373](https://doi.org/10.1086/673373)

Brandt, T. D. 2024, Astrometry as a Tool for Discovering and Weighing Faint Companions to Nearby Stars, *Publications of the Astronomical Society of the Pacific*, 136, 073001, doi: [10.1088/1538-3873/ad59c5](https://doi.org/10.1088/1538-3873/ad59c5)

Bresler, Y., Basu, S., & Couvreur, C. 2000, Hilbert spaces and least squares methods for signal processing, Unpublished lecture notes

Cardoso, J.-F. 2010, Precision cosmology with the cosmic microwave background, *IEEE Signal Processing Magazine*, 27, 55, doi: [10.1109/MSP.2009.934715](https://doi.org/10.1109/MSP.2009.934715)

Catanzarite, J., Law, N., & Shao, M. 2008, in *Optical and Infrared Interferometry*, Vol. 7013, SPIE, 825–835

Chiavassa, A., Haubois, X., Young, J. S., et al. 2010, Radiative hydrodynamics simulations of red supergiant stars. II. Simulations of convection on Betelgeuse match interferometric observations, *A&A*, 515, A12, doi: [10.1051/0004-6361/200913907](https://doi.org/10.1051/0004-6361/200913907)

Chiavassa, A., Kudritzki, R., Davies, B., Freytag, B., & de Mink, S. E. 2022, Probing red supergiant dynamics through photo-center displacements measured by Gaia, *A&A*, 661, L1, doi: [10.1051/0004-6361/202243568](https://doi.org/10.1051/0004-6361/202243568)

Christiansen, J. 2025, in *American Astronomical Society Meeting Abstracts*, Vol. 245, American Astronomical Society Meeting Abstracts #245, 234.05

Cowan, N. B., Fuentes, P. A., & Haggard, H. M. 2013a, Light curves of stars and exoplanets: estimating inclination, obliquity and albedo, *Monthly Notices of the Royal Astronomical Society*, 434, 2465, doi: [10.1093/mnras/stt1191](https://doi.org/10.1093/mnras/stt1191)

Cowan, N. B., Fuentes, P. A., & Haggard, H. M. 2013b, Light curves of stars and exoplanets: estimating inclination, obliquity and albedo, *Monthly Notices of the Royal Astronomical Society*, 434, 2465, doi: [10.1093/mnras/stt1191](https://doi.org/10.1093/mnras/stt1191)

Damiano, M., Burr, Z., Hu, R., Burt, J., & Kataria, T. 2025, Effects of Planetary Mass Uncertainties on the Interpretation of the Reflectance Spectra of Earth-like Exoplanets, *The Astronomical Journal*, 169, 97, doi: [10.3847/1538-3881/ada610](https://doi.org/10.3847/1538-3881/ada610)

Davenport, J. R. A., Hebb, L., & Hawley, S. L. 2015, DETECTING DIFFERENTIAL ROTATION AND STARSPOT EVOLUTION ON THE M DWARF GJ 1243 WITH KEPLER, *The Astrophysical Journal*, 806, 212, doi: [10.1088/0004-637X/806/2/212](https://doi.org/10.1088/0004-637X/806/2/212)

Dholakia, S., & Pope, B. J. S. 2025, Analytic Interferometry of Rotating Stellar Surfaces, <https://arxiv.org/abs/2509.25433>

Donoho, D. L., & Stark, P. B. 1989, Uncertainty Principles and Signal Recovery, *SIAM Journal on Applied Mathematics*, 49, 906, doi: [10.1137/0149053](https://doi.org/10.1137/0149053)

Dorren, J. D. 1987, A New Formulation of the Starspot Model, and the Consequences of Starspot Structure, *ApJ*, 320, 756, doi: [10.1086/165593](https://doi.org/10.1086/165593)

Eker, Z. 1996, Synthetic Light Curves of Spotted Stars: Unique or Not Unique?, *ApJ*, 473, 388, doi: [10.1086/178153](https://doi.org/10.1086/178153)

Eriksson, U., & Lindegren, L. 2007, Limits of ultra-high-precision optical astrometry - Stellar surface structures, *A&A*, 476, 1389, doi: [10.1051/0004-6361:20078031](https://doi.org/10.1051/0004-6361:20078031)

Farr, B., Farr, W. M., Cowan, N. B., Haggard, H. M., & Robinson, T. 2018, exocartographer: A Bayesian Framework for Mapping Exoplanets in Reflected Light, *The Astronomical Journal*, 156, 146, doi: [10.3847/1538-3881/aad775](https://doi.org/10.3847/1538-3881/aad775)

Gaia Collaboration, Prusti, T., de Bruijne, J. H. J., et al. 2016, The Gaia mission, *A&A*, 595, A1, doi: [10.1051/0004-6361/201629272](https://doi.org/10.1051/0004-6361/201629272)

Guyon, O., Bendek, E., Ammons, M., et al. 2011, in *Society of Photo-Optical Instrumentation Engineers (SPIE) Conference Series*, Vol. 8151, Techniques and Instrumentation for Detection of Exoplanets V, ed. S. Shaklan, 81510S, doi: [10.1117/12.894302](https://doi.org/10.1117/12.894302)

Guyon, O., Bendek, E., Ammons, S. M., et al. 2012, in *Society of Photo-Optical Instrumentation Engineers (SPIE) Conference Series*, Vol. 8442, *Space Telescopes and Instrumentation 2012: Optical, Infrared, and Millimeter Wave*, ed. M. C. Clampin, G. G. Fazio, H. A. MacEwen, & J. M. Oschmann, Jr., 84420K, doi: [10.1117/12.927196](https://doi.org/10.1117/12.927196)

Haggard, H. M., & Cowan, N. B. 2018, Analytic reflected light curves for exoplanets, *Monthly Notices of the Royal Astronomical Society*, 478, 371, doi: [10.1093/mnras/sty1019](https://doi.org/10.1093/mnras/sty1019)

Harmon, R., & Crews, L. 2000, Imaging Stellar Surfaces via Matrix Light-Curve Inversion, *Astronomical Journal - ASTRON J*, 120, 3274, doi: [10.1086/316882](https://doi.org/10.1086/316882)

Kipping, D. M. 2012, An analytic model for rotational modulations in the photometry of spotted stars, *Monthly Notices of the Royal Astronomical Society*, 427, 2487, doi: [10.1111/j.1365-2966.2012.22124.x](https://doi.org/10.1111/j.1365-2966.2012.22124.x)

Kovari, Z., & Bartus, J. 1997, Testing the stability and reliability of starspot modelling., *A&A*, 323, 801

Lammers, C., & Winn, J. N. 2025, On the Exoplanet Yield of Gaia Astrometry, arXiv e-prints, arXiv:2511.04673, doi: [10.48550/arXiv.2511.04673](https://doi.org/10.48550/arXiv.2511.04673)

Libby-Roberts, J. E., Schutte, M., Hebb, L., et al. 2023, An In-depth Look at TOI-3884b: A Super-Neptune Transiting an M4Dwarf with Persistent Starspot Crossings, *The Astronomical Journal*, 165, 249, doi: [10.3847/1538-3881/accc2f](https://doi.org/10.3847/1538-3881/accc2f)

Luger, R., Agol, E., Foreman-Mackey, D., et al. 2019, starry: Analytic Occultation Light Curves, *The Astronomical Journal*, 157, 64, doi: [10.3847/1538-3881/aae8e5](https://doi.org/10.3847/1538-3881/aae8e5)

Luger, R., Foreman-Mackey, D., & Hedges, C. 2021a, Mapping Stellar Surfaces. II. An Interpretable Gaussian Process Model for Light Curves, *The Astronomical Journal*, 162, 124, doi: [10.3847/1538-3881/abfdb9](https://doi.org/10.3847/1538-3881/abfdb9)

Luger, R., Foreman-Mackey, D., Hedges, C., & Hogg, D. W. 2021b, Mapping Stellar Surfaces. I. Degeneracies in the Rotational Light-curve Problem, *The Astronomical Journal*, 162, 123, doi: [10.3847/1538-3881/abfdb8](https://doi.org/10.3847/1538-3881/abfdb8)

Makadia, A., & Daniilidis, K. 2003, in 2003 IEEE Computer Society Conference on Computer Vision and Pattern Recognition, 2003. Proceedings., Vol. 2, II–217, doi: [10.1109/CVPR.2003.1211473](https://doi.org/10.1109/CVPR.2003.1211473)

Makarov, V. V., Beichman, C. A., Catanzarite, J. H., et al. 2009, Starspot Jitter in Photometry, Astrometry, and Radial Velocity Measurements, *ApJL*, 707, L73, doi: [10.1088/0004-637X/707/1/L73](https://doi.org/10.1088/0004-637X/707/1/L73)

Makarov, V. V., Parker, D., & Ulrich, R. K. 2010, Astrometric Jitter of the Sun as a Star, *ApJ*, 717, 1202, doi: [10.1088/0004-637X/717/2/1202](https://doi.org/10.1088/0004-637X/717/2/1202)

Masuda, K., & Winn, J. N. 2020, On the Inference of a Star's Inclination Angle from its Rotation Velocity and Projected Rotation Velocity, *AJ*, 159, 81, doi: [10.3847/1538-3881/ab65be](https://doi.org/10.3847/1538-3881/ab65be)

McQuillan, A., Mazeh, T., & Aigrain, S. 2014, Rotation Periods of 34,030 Kepler Main-sequence Stars: The Full Autocorrelation Sample, *ApJS*, 211, 24, doi: [10.1088/0067-0049/211/2/24](https://doi.org/10.1088/0067-0049/211/2/24)

Mennesson, B., Belikov, R., Por, E., et al. 2024, Current laboratory performance of starlight suppression systems and potential pathways to desired Habitable Worlds Observatory exoplanet science capabilities, *Journal of Astronomical Telescopes, Instruments, and Systems*, 10, 035004, doi: [10.1117/1.JATIS.10.3.035004](https://doi.org/10.1117/1.JATIS.10.3.035004)

Meunier, N., & Lagrange, A. M. 2022, A new estimation of astrometric exoplanet detection limits in the habitable zone around nearby stars, *A&A*, 659, A104, doi: [10.1051/0004-6361/202142702](https://doi.org/10.1051/0004-6361/202142702)

Meurer, A., Smith, C. P., Paprocki, M., et al. 2017, SymPy: symbolic computing in Python, *PeerJ Computer Science*, 3, e103, doi: [10.7717/peerj-cs.103](https://doi.org/10.7717/peerj-cs.103)

Monnier, J. D., Zhao, M., Pedretti, E., et al. 2007, Imaging the Surface of Altair, *Science*, 317, 342, doi: [10.1126/science.1143205](https://doi.org/10.1126/science.1143205)

Morris, B. M., Agol, E., Davenport, J. R., & Hawley, S. L. 2018, Spotting stellar activity cycles in Gaia astrometry, *Monthly Notices of the Royal Astronomical Society*, 476, 5408

Nichols-Fleming, F., & Blackman, E. G. 2019, Determination of the star-spot covering fraction as a function of stellar age from observational data, *Monthly Notices of the Royal Astronomical Society*, 491, 2706, doi: [10.1093/mnras/stz3197](https://doi.org/10.1093/mnras/stz3197)

Oppenheim, A. 1993, *Digital Signal Processing* (PRENTICE-HALL OF INDIA). <https://books.google.com/books?id=vSzuVLBbp6cC>

Painter, K. E., Bowler, B. P., Franson, K., Becker, J. C., & Burt, J. A. 2025, Astrometric Accelerations of Provisional Targets for the Habitable Worlds Observatory, *The Astronomical Journal*, 170, 147, doi: [10.3847/1538-3881/ade442](https://doi.org/10.3847/1538-3881/ade442)

Parks, J. R., White, R. J., Baron, F., et al. 2021, Interferometric Imaging of  $\lambda$  Andromedae: Evidence of Starspots and Rotation, *The Astrophysical Journal*, 913, 54, doi: [10.3847/1538-4357/abb670](https://doi.org/10.3847/1538-4357/abb670)

Perryman, M. 2018, *The Exoplanet Handbook*

Rackham, B. V., Apai, D., & Giampapa, M. S. 2018, The Transit Light Source Effect: False Spectral Features and Incorrect Densities for M-dwarf Transiting Planets, *The Astrophysical Journal*, 853, 122, doi: [10.3847/1538-4357/aaa08c](https://doi.org/10.3847/1538-4357/aaa08c)

Rackham, B. V., Espinoza, N., Berdyugina, S. V., et al. 2023, The effect of stellar contamination on low-resolution transmission spectroscopy: needs identified by NASA's Exoplanet Exploration Program Study Analysis Group 21, *RAS Techniques and Instruments*, 2, 148, doi: [10.1093/rasti/rzad009](https://doi.org/10.1093/rasti/rzad009)

Ranalli, P., Hobbs, D., & Lindegren, L. 2018, Astrometry and exoplanets in the Gaia era: a Bayesian approach to detection and parameter recovery, *A&A*, 614, A30, doi: [10.1051/0004-6361/201730921](https://doi.org/10.1051/0004-6361/201730921)

Rauscher, E., Suri, V., & Cowan, N. B. 2018, A More Informative Map: Inverting Thermal Orbital Phase and Eclipse Light Curves of Exoplanets, *The Astronomical Journal*, 156, 235, doi: [10.3847/1538-3881/aae57f](https://doi.org/10.3847/1538-3881/aae57f)

Reylé, C., Jardine, K., Fouqué, P., et al. 2021, The 10 parsec sample in the Gaia era, *A & A*, 650, A201, doi: [10.1051/0004-6361/202140985](https://doi.org/10.1051/0004-6361/202140985)

Roettenbacher, R. M., Monnier, J. D., Korhonen, H., et al. 2017, Contemporaneous Imaging Comparisons of the Spotted Giant  $\sigma$  Geminorum Using Interferometric, Spectroscopic, and Photometric Data, *ApJ*, 849, 120, doi: [10.3847/1538-4357/aa8ef7](https://doi.org/10.3847/1538-4357/aa8ef7)

Russell, H. N. 1906, On the light variations of asteroids and satellites, *ApJ*, 24, 1, doi: [10.1086/141361](https://doi.org/10.1086/141361)

Sagynbayeva, S., Farr, W. M., Morris, B. M., & Luger, R. 2025, Polka-dotted Stars: A Hierarchical Model for Mapping Stellar Surfaces Using Occultation Light Curves and the Case of TOI-3884, *The Astrophysical Journal*, 990, 32, doi: [10.3847/1538-4357/adf6be](https://doi.org/10.3847/1538-4357/adf6be)

Sakurai, J. J., & Napolitano, J. 2020, Modern Quantum Mechanics, 3rd edn. (Cambridge University Press)

Shao, M., Marcy, G., Catanzarite, J. H., et al. 2009, in astro2010: The Astronomy and Astrophysics Decadal Survey, Vol. 2010, 271, doi: [10.48550/arXiv.0904.0965](https://doi.org/10.48550/arXiv.0904.0965)

Shapiro, A. I., Solanki, S. K., & Krivova, N. A. 2021, Predictions of Astrometric Jitter for Sun-like Stars. I. The Model and Its Application to the Sun as Seen from the Ecliptic, *The Astrophysical Journal*, 908, 223, doi: [10.3847/1538-4357/abd630](https://doi.org/10.3847/1538-4357/abd630)

Silva, A. V. R. 2003, Method for Spot Detection on Solar-like Stars, *The Astrophysical Journal*, 585, L147, doi: [10.1086/374324](https://doi.org/10.1086/374324)

Solanki, S. 2003, Sunspots: An overview, *Astronomy and Astrophysics Review*, 11, 153, doi: [10.1007/s00159-003-0018-4](https://doi.org/10.1007/s00159-003-0018-4)

Sowmya, K., Némec, N.-E., Shapiro, A. I., et al. 2022, Predictions of Astrometric Jitter for Sun-like Stars. III. Fast Rotators, *The Astrophysical Journal*, 934, 146, doi: [10.3847/1538-4357/ac79b3](https://doi.org/10.3847/1538-4357/ac79b3)

Sowmya, K., Némec, N.-E., Shapiro, A. I., et al. 2021, Predictions of Astrometric Jitter for Sun-like Stars. II. Dependence on Inclination, Metallicity, and Active-region Nesting, *The Astrophysical Journal*, 919, 94, doi: [10.3847/1538-4357/ac111b](https://doi.org/10.3847/1538-4357/ac111b)

Stapelfeldt, K., & Mamajek, E. 2025, NASA Exoplanet Exploration Program (ExEP) Science Gap List, arXiv e-prints, arXiv:2507.18665, doi: [10.48550/arXiv.2507.18665](https://doi.org/10.48550/arXiv.2507.18665)

Stefánsson, G., Mahadevan, S., Winn, J. N., et al. 2025, Gaia-4b and 5b: Radial Velocity Confirmation of Gaia Astrometric Orbital Solutions Reveal a Massive Planet and a Brown Dwarf Orbiting Low-mass Stars, *The Astronomical Journal*, 169, 107, doi: [10.3847/1538-3881/ada9e1](https://doi.org/10.3847/1538-3881/ada9e1)

Strassmeier, K. G. 2009, Starspots, *A&A Rv*, 17, 251, doi: [10.1007/s00159-009-0020-6](https://doi.org/10.1007/s00159-009-0020-6)

Taaki, J., Corrales, L., & Hero, A. 2025, Identifiability of Rotating Stellar Surfaces from Astrometric Jitter, arXiv e-prints, arXiv:2511.07706, doi: [10.48550/arXiv.2511.07706](https://doi.org/10.48550/arXiv.2511.07706)

Tamburo, P., Yee, S. W., García-Mejía, J., et al. 2025, Spot-crossing Variations Confirm a Misaligned Orbit for a Planet Transiting an M Dwarf, *AJ*, 170, 200, doi: [10.3847/1538-3881/adf72f](https://doi.org/10.3847/1538-3881/adf72f)

Vogt, S. S., Penrod, G. D., & Hatzes, A. P. 1987, Doppler Images of Rotating Stars Using Maximum Entropy Image Reconstruction, *ApJ*, 321, 496, doi: [10.1086/165647](https://doi.org/10.1086/165647)

Walkowicz, L. M., Basri, G., & Valenti, J. A. 2013, THE INFORMATION CONTENT IN ANALYTIC SPOT MODELS OF BROADBAND PRECISION LIGHT CURVES, *The Astrophysical Journal Supplement Series*, 205, 17, doi: [10.1088/0067-0049/205/2/17](https://doi.org/10.1088/0067-0049/205/2/17)

Wright, J., & Gaudi, B. 2012, Exoplanet Detection Methods, Planets, Stars and Stellar Systems. Volume 3: Solar and Stellar Planetary Systems, doi: [10.1007/978-90-481-8818-5\\_59](https://doi.org/10.1007/978-90-481-8818-5_59)

Zhao, M., Monnier, J. D., Pedretti, E., et al. 2009, IMAGING AND MODELING RAPIDLY ROTATING STARS:  $\alpha$  CEPHEI AND  $\alpha$  OPHIUCHI, *The Astrophysical Journal*, 701, 209, doi: [10.1088/0004-637X/701/1/209](https://doi.org/10.1088/0004-637X/701/1/209)